**ORIGINAL ARTICLE**

# Higher order phase-field modeling of brittle fracture *via* isogeometric analysis

Luigi Greco[1] · Alessia Patton[2] · Matteo Negri[3] · Alessandro Marengo[4] · Umberto Perego[5] · Alessandro Reali[1] 

**Abstract**

The evolution of brittle fracture in a material can be conveniently investigated by means of the phase-field technique introducing a smooth crack density functional. Following *Borden et al. (2014)*, two distinct types of phase-field functional are considered: (i) a second-order model and (ii) a fourth-order one. The latter approach involves the bi-Laplacian of the phase field and therefore the resulting Galerkin form requires continuously differentiable basis functions: a condition we easily fulfill *via* Isogeometric Analysis. In this work, we provide an extensive comparison of the considered formulations performing several tests that progressively increase the complexity of the crack patterns. To measure the fracture length necessary in our accuracy evaluations, we propose an image-based algorithm that features an automatic skeletonization technique able to track complex fracture patterns. In all numerical results, damage irreversibility is handled in a straightforward and rigorous manner using the Projected Successive Over-Relaxation algorithm that is suitable to be adopted for both phase-field formulations since it can be used in combination with higher continuity isogeometric discretizations. Based on our results, the fourth-order approach provides higher rates of convergence and a greater accuracy. Moreover, we observe that fourth- and second-order models exhibit a comparable accuracy when the former methods employ a mesh-size approximately two times larger, entailing a substantial reduction of the computational effort.

**Keywords** High order phase-field modeling · Isogeometric analysis · Brittle fracture · Linear complementarity problem · Projected successive over-relaxation algorithm · Staggered scheme

## 1 Introduction

The prevention of fracture-induced failure is a major constraint in engineering design. The numerical simulation of fracture has the potential to offer a decision-making tool within the engineering design process, ultimately able to reduce the necessity of expensive and time-consuming experimental tests. As a consequence, a wide variety of fracture numerical models have been proposed, among which the phase-field method has gained a lot of popularity as it can elegantly simulate complex crack patterns (including, e.g., crack initiation, propagation, merging, and branching)

---

Luigi Greco and Alessia Patton contributed equally to this work.

✉ Alessandro Reali
  alessandro.reali@unipv.it

  Luigi Greco
  luigi.greco01@universitadipavia.it

  Alessia Patton
  alessia.patton@unibw.de

  Matteo Negri
  matteo.negri@unipv.it

  Alessandro Marengo
  alessandro.marengo@polimi.it

  Umberto Perego
  umberto.perego@polimi.it

[1] Department of Civil Engineering and Architecture, University of Pavia, Via A. Ferrata 3, 27100 Pavia, Italy

[2] Department of Civil Engineering and Environmental sciences, Universität der Bundeswehr München, Werner-Heisenberg-Weg 39, 85577 Neubiberg, Germany

[3] Department of Mathematics F. Casorati, University of Pavia, Via A. Ferrata 5, 27100 Pavia, Italy

[4] Tetra Pak Packaging Solutions, Via Delfini 1, 41100 Modena, Italy

[5] Department of Civil and Environmental Engineering, Politecnico di Milano, Piazza L. Da Vinci 32, 20133 Milan, Italy

🖄 Springer

and automatically tracks the fracture path without needing remeshing techniques. The corner stone of this method is the work of Griffith [1], where fracture is studied from an energy point of view: a crack propagates when the energy release rate reaches a critical value. Based on this work, Francfort et al. [2] proposed a variational model based on energy minimization. After that, Bourdin et al. [3] introduced a phase-field variable to regularize the sharp interface and it was proven [4, 5] that the smooth problem converges to the sharp one when the parameter $l_0$, representing the length scale of the regularization, tends to zero. Miehe et al. [6] introduced a thermodynamically consistent framework for phase-field models of quasi-static crack propagation in elastic solids, developing incremental variational principles. In this work, the authors also introduced the idea of fracture irreversibility, imposed by a strain history variable. The idea was to apply the irreversibility constraint on the driving force and through the Strain History Variable technique. Among other strategies to impose the irreversibility constraint, Gerasimov and De Lorenzis [7] proposed a method based on a penalty technique. The idea is to enrich the dissipated energy functional with an integral term depending on a parameter that penalizes negative phase-field increments. The critical point of this method is that this penalty parameter needs to be calibrated, with such a calibration depending upon the optimal phase-field profile. In this work, the Projected Successive Over-Relaxation algorithm (PSOR) utilized by Marengo et al. [8] to impose irreversibility for low-order phase-field brittle fracture formulations is considered in the context of high-order formulations. This algorithm relies on an iterative scheme of Gauss–Seidel type for the solution of linear systems and takes a suitable projection that allows for a rigorous enforcement of the irreversibility of damage, therefore providing direct applicability and computational efficiency, without needing to calibrate any penalty parameter.

In 2012, Borden et al. [9] extended the brittle quasi-static model proposed in [6] to the dynamic case and showed that the phase-field method is able to capture branching and coalescence phenomena also in dynamics. Later, Borden et al. [10] proposed a fourth-order phase-field problem, for which Negri [11] rigorously proved its Γ-convergence. The increased regularity of this high-order phase-field profile leads to increased accuracy of the strain energy implying that stresses will be more accurate with respect to a low-order formulation. To discretize within a Galerkin framework this functional that involves the bi-Laplacian of the phase-field, at least $C^1$-continuous shape functions are required. This can be relatively easily achieved in the context of Isogeometric Analysis (IgA), introduced by Hughes et al. [12] in 2005 with the original aim to bridge the gap between Finite Elements Analysis and Computer Aided Design. Starting from the pioneering work of Borden et al. [10], the phase-field fourth-order model, for which IgA represents a natural modeling framework able to easily handle its high-order continuity requirements, has attracted a lot of attention given its ability to represent the crack pattern with a coarser mesh with respect to low-order formulations. For example, Nguyen-Thanh et al. [13] applied it to polycrystalline materials using a novel approach based on the isogeometric meshfree collocation method, while Schillinger et al. [14] considered an isogeometric hybrid collocation-Galerkin formulation that provides a consistent way of weakly enforcing Neumann boundary conditions and multi-patch interface constraints. Nguyen et al. [15] focused on a phase-field higher-order model using a combination of IgA and the Virtual Uncommon-Knot-Inserted Master–Slave algorithm, suitable to deal with non-conforming meshes and multi-patch problems, to locally refine the area where the crack is expected to propagate. Goswami et al. [16] instead proposed an adaptive re-meshing technique that uses T-splines and features an $h$-refinement strategy whose activation is based on a threshold value of the phase field, while Proserpio et al. [17] introduced a multi-patch technique to study higher-order phase-field methods for shells based on a multistep predictor–corrector algorithm for adaptive local refinement using LR NURBS.

In this work, we provide an in-depth comparison of low- and high-order formulations for phase-field brittle fracture that underlines the computational advantages of high-order models discretized within an isogeometric framework. To compare the two models, a quantitative accuracy study that relies on the evaluation of the effective toughness is performed following Borden et al. [10]. However, this approach is affected by the measurement of the fracture length, whose evaluation is not straightforward in the case of complicated phase-field paths, such as curved or branched ones. However, we can handle such complex patterns using an image-based algorithm featuring an automatic skeletonization technique of the fracture. In all numerical tests, irreversibility is rigorously imposed using the PSOR algorithm that can be directly combined with the isogeometric discretization of the considered high-order functional. All our numerical tests confirm the superior behavior of the fourth-order formulation. The structure of the paper is as follows. In Sect. 2, we briefly present the considered second- and fourth-order phase-field formulations that account for a different damaging behavior in tension and compression as in [18] focusing on a quasi-static evolution. Then, in Sect. 3 we introduce the proposed numerical approximation strategy focusing on the rigorous solution of the phase-field problem using the PSOR algorithm that finds direct application within the adopted isogeometric discretization. Section 4 provides extensive numerical testing that showcases the advantages of the fourth-order formulation over the second-order one. Given the evolutionary nature of the phase-field problem, particular attention is devoted on possible strategies to impose a phase-field initial condition, as detailed in Appendix A, while an extensive description of the proposed crack tracking

image-based algorithm can be found in Appendix B. Finally, we draw our conclusions in Sect. 5.

# 2 Phase-field variational formulations

In this section, the considered phase-field formulations are shortly summarized. Following [10], we define the reference domain $\Omega \subset \mathbb{R}^N$ (where $N$ is the dimension of the problem). Dirichlet boundary conditions are applied on $\partial\Omega_D \subseteq \partial\Omega$, while Neumann boundary conditions are given on $\partial\Omega_N \subseteq \partial\Omega$ with $\partial\Omega_D \cup \partial\Omega_N = \partial\Omega$ and $\partial\Omega_D \cap \partial\Omega_N = \emptyset$. Therefore, the admissible deformations $\mathbf{u}$ belong to the space:

$$\mathcal{U}_\mathbf{u} := \{\mathbf{u} \in H^1(\Omega;\mathbb{R}^N) : \mathbf{u} = \bar{\mathbf{u}} \text{ on } \partial\Omega_D\},$$

while the phase-field function d, which may be regarded as a smooth regularization of the sharp crack, belongs to the set

$$\mathcal{U}_\mathrm{d}^{ii} := H^1(\Omega;[0,+\infty)) = \{\mathrm{d} \in H^1(\Omega) : \mathrm{d} \geq 0\},$$
$$\mathcal{U}_\mathrm{d}^{iv} := H^2(\Omega;[0,+\infty)) = \{\mathrm{d} \in H^2(\Omega) : \mathrm{d} \geq 0\},$$

respectively, for second-order and fourth-order formulations.

Strictly speaking, the phase field d should take values in [0, 1] (with d = 0 and d = 1 corresponding to the unbroken and fully broken material states, respectively). Here we are choosing instead d $\geq$ 0 which, *a priori*, allows for d > 1. However, in the evolution the staggered scheme will select (by optimality) a phase-field d taking values in [0, 1]. Therefore, we adopt the weaker constraint d $\geq$ 0 which is more convenient from both the mathematical and numerical point of view.

The fact that the evolution of the phase-field d will take values in [0, 1] is, roughly speaking, related to the optimal profile in Γ-convergence (see below).

## 2.1 Energy functionals

We assume small strains, i.e., $\varepsilon = \nabla^s \mathbf{u}$ (with $\nabla^s$ denoting the symmetric part of the gradient operator) and therefore, for quasi-static brittle fracture, the total energy functionals (for second- and fourth-order formulations) take the form:

$$\Pi^{ii,iv}(\mathbf{u}, \mathrm{d}) := \mathcal{E}(\mathbf{u}, \mathrm{d}) + G_c \mathcal{D}^{ii,iv}(\mathrm{d}) - \mathcal{W}^{\text{ext}}(\mathbf{u}). \tag{1}$$

Here, $\mathcal{W}^{\text{ext}}(\mathbf{u}) := \int_\Omega \mathbf{b} \cdot \mathbf{u} \, \mathrm{d}\Omega + \int_{\partial\Omega_N} \mathbf{t} \cdot \mathbf{u} \, \mathrm{d}\partial\Omega$ is the usual external work functional, where $\mathbf{b}$ and $\mathbf{t}$ are body and surface force densities, respectively. In Eq. (1), $\mathcal{E}(\mathbf{u}, \mathrm{d})$ is the elastic strain energy and is defined as

$$\mathcal{E}(\mathbf{u}, \mathrm{d}) := \int_\Omega \psi(\varepsilon(\mathbf{u}), \mathrm{d}) \, \mathrm{d}\Omega = \int_\Omega \left( \omega(\mathrm{d}) \, \psi_0^+(\varepsilon(\mathbf{u})) + \psi_0^-(\varepsilon(\mathbf{u})) \right) \mathrm{d}\Omega, \tag{2}$$

where, as proposed in [5, 18], $\psi_0^\pm$ are taken, respectively, as

$$\psi_0^+(\varepsilon(\mathbf{u})) := \frac{1}{2}\left( K(\varepsilon_v^+)^2 + \mu|\varepsilon_d|^2 \right), \qquad \psi_0^-(\varepsilon(\mathbf{u})) := \frac{1}{2}\left( K(\varepsilon_v^-)^2 \right). \tag{3}$$

The volumetric strain $\varepsilon_v$ is defined as $\varepsilon_v = \varepsilon : \mathbf{I}$, where $\mathbf{I}$ is the identity tensor and $\varepsilon_v^\pm := \langle \varepsilon_v \rangle_\pm$ denote its positive and negative part, while $\varepsilon_d := \varepsilon - \frac{1}{N}\varepsilon_v \mathbf{I}$ is the deviatoric strain; $K > 0$ and $\mu > 0$ are the bulk and shear moduli, respectively. The monotonically decreasing function $\omega(\mathrm{d}) = (1 - \mathrm{d})^2 + \eta$ describes the degradation of the stored energy due to evolving damage and satisfies the following properties: $\omega(0) = 1 + \eta$, $\omega(1) = 0$, and $\omega'(1) = \eta$, while $\eta > 0$, with $\eta \approx 0$, circumvents the full degradation of $\psi_0^+$ by leaving an artificial elastic remainder in the positive part of the free energy when d approaches the limit value 1, see, e.g., [6].

In Eq. (1), the term $\mathcal{D}^{ii,iv}$ denotes the phase-field energy functionals:

$$\mathcal{D}^{ii}(\mathrm{d}) := \int_\Omega \frac{1}{2l_0}\left( \mathrm{d}^2 + l_0^2|\nabla\mathrm{d}|^2 \right) \mathrm{d}\Omega, \tag{4a}$$

$$\mathcal{D}^{iv}(\mathrm{d}) := \int_\Omega \frac{1}{2l_0}\left( \mathrm{d}^2 + \frac{l_0^2}{2}|\nabla\mathrm{d}|^2 + \frac{l_0^4}{16}\left(\nabla^2\mathrm{d}\right)^2 \right) \mathrm{d}\Omega, \tag{4b}$$

where $0 \leq l_0 \ll 1$ is the internal (phase-field) length, while $\nabla$ denotes the gradient and $\nabla^2$ the Laplacian operators. In the above integrals, the coefficients are chosen in such a way that the phase-field energy provides an approximation of the $(N-1)$-dimensional measure of the crack (see, e.g., [11]); the product of $\mathcal{D}^{ii,iv}$ and the material toughness $G_c > 0$ gives the energy dissipated during fracture propagation.

### 2.1.1 Optimal profiles

In this subsection, we briefly recall the optimal profiles of the phase field. For second order formulations the optimal profile $\mathrm{d}_{ii}$ is the minimizer of the energy $\int_\mathbb{R} \left( l_0^{-1}\mathrm{d}^2 + l_0|\mathrm{d}'|^2 \right) \mathrm{d}x$ under the assumptions $\mathrm{d}(0) = 1$ and $\mathrm{d}(x) \to 0$ as $|x| \to \infty$. The solution (plotted in Fig. 1) is

$$\mathrm{d}_{ii}(x) = \exp\left( \frac{-|x|}{l_0} \right),$$

which is easily computed using the Euler–Lagrange equation:

$$l_0^2\mathrm{d}''(x) - \mathrm{d}(x) = 0 \quad \text{for } x > 0.$$

Instead, for the considered fourth-order theory, the optimal profile is obtained minimising the energy $\int_\mathbb{R} \left( l_0^{-1}\mathrm{d}^2 + \frac{1}{2}l_0|\mathrm{d}'|^2 + \frac{1}{16}l_0^3|\mathrm{d}''|^2 \right) \mathrm{d}x$ under the assumptions $\mathrm{d}(0) = 1$, $\mathrm{d}'(0) = 0$ and $\mathrm{d}(x) \to 0$, $\mathrm{d}'(x) \to 0$ as $|x| \to \infty$. The closed-form solution is
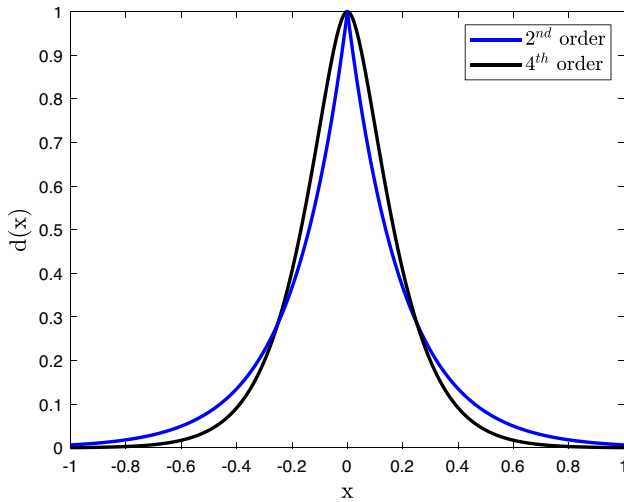
**Fig. 1** Second-order *versus* fourth-order phase-field 1D profiles

$$d_{iv}(x) = \exp\left(\frac{-|2x|}{l_0}\right)\left(1 + \frac{|2x|}{l_0}\right),$$

which is smoother than $d_{ii}$ (as it may be noticed in Fig. 1) and is computed by means of the Euler–Lagrange equation:

$$l_0^4\, d^{(iv)}(x) - 8l_0^2\, d''(x) + 16\, d(x) = 0 \quad \text{for } x > 0.$$

## 2.2 Variational formulations within a quasi-static evolution

The evolution $t \rightarrow (\mathbf{u}(t), d(t)) \in \mathcal{U}_\mathbf{u} \times \mathcal{U}_d^{ii,iv}$ is characterized (at least in the steady state regime) by two ingredients: equilibrium and power identity (or, equivalently, energy conservation).

### 2.2.1 Evolution in terms of energy variations

For simplicity we assume that the external forces are independent of time. For the displacement field $\mathbf{u}$, equilibrium, in terms of energy variations, reads $\partial_\mathbf{u}\Pi^{ii,iv}(\mathbf{u}, d)[\delta\mathbf{u}] = 0$ for every admissible variation $\delta\mathbf{u} \in \{H^1(\Omega;\mathbb{R}^N) : \delta\mathbf{u} = \mathbf{0} \text{ in } \partial\Omega_D\}$. For the phase-field d, equilibrium is slightly different, as indeed, by irreversibility it is equivalent to $\partial_d\Pi^{ii,iv}(\mathbf{u}, d)[\delta d] \geq 0$ for every admissible variation $\delta d \geq 0$. Taking the time derivative of the energy (assuming differentiability) the power identity reads

$$\dot{\Pi}^{ii,iv} = \frac{d\Pi^{ii,iv}}{dt}(\mathbf{u}, d) = \partial_\mathbf{u}\Pi^{ii,iv}(\mathbf{u}, d)[\dot{\mathbf{u}}] + \partial_d\Pi^{ii,iv}(\mathbf{u}, d)[\dot{d}] = 0.$$

As $\dot{\mathbf{u}} = \mathbf{0}$ on $\partial\Omega_D$ it follows that $\partial_\mathbf{u}\Pi^{ii,iv}(\mathbf{u}, d)[\dot{\mathbf{u}}] = 0$ and thus the above identity boils down to

$$\partial_d\Pi^{ii,iv}(\mathbf{u}, d)[\dot{d}] = 0.$$

In conclusion, (in the steady state regime) the evolution $t \rightarrow (\mathbf{u}(t), d(t))$ is characterized by the following system:

$$\begin{cases} \partial_\mathbf{u}\Pi^{ii,iv}(\mathbf{u}, d) = \mathbf{0}, \\ \partial\Pi^{ii,iv}(\mathbf{u}, d) \geq 0, \\ \partial_d\Pi^{ii,iv}(\mathbf{u}, d)[\dot{d}] = 0, \quad \dot{d} \geq 0. \end{cases} \tag{5}$$

### 2.2.2 Evolution in terms of PDEs

Clearly

$$\partial_\mathbf{u}\Pi^{ii,iv}(\mathbf{u}, d)[\delta\mathbf{u}] = \int_\Omega \partial_\varepsilon\psi(\varepsilon(\mathbf{u}), d){:}\varepsilon(\delta\mathbf{u})\, d\Omega$$
$$- \int_\Omega \mathbf{b} \cdot \delta\mathbf{u}\, d\Omega - \int_{\partial\Omega_N} \mathbf{t} \cdot \delta\mathbf{u}\, d\partial\Omega,$$

and thus the equilibrium of $\mathbf{u}$ is equivalent to the system of PDEs

$$\begin{cases} \boldsymbol{\nabla} \cdot \boldsymbol{\sigma} + \mathbf{b} = \mathbf{0} & \text{in } \Omega \\ \mathbf{u} = \bar{\mathbf{u}} & \text{on } \partial\Omega_D \\ \boldsymbol{\sigma} \cdot \mathbf{n} = \mathbf{t} & \text{on } \partial\Omega_N, \end{cases} \tag{6}$$

where the phase-field stress tensor $\boldsymbol{\sigma}$ is given by

$$\boldsymbol{\sigma} := \partial_\varepsilon\psi(\varepsilon(\mathbf{u}), d) = \omega(d)\, \partial_\varepsilon\psi_0^+(\varepsilon(\mathbf{u}))+$$
$$\partial_\varepsilon\psi_0^-(\varepsilon(\mathbf{u})) = \boldsymbol{\sigma}^+ + \boldsymbol{\sigma}^-.$$

For the phase-field it is convenient to distinguish between $\Pi^{ii}$ and $\Pi^{iv}$. For $\Pi^{ii}$ we have that the variational form is (see also [8, §A])

$$\partial_d\Pi^{ii}(\mathbf{u}, d)[\delta d] = \int_\Omega -2(1 - d)\psi_0^+(\varepsilon(\mathbf{u}))\delta d\, d\Omega$$
$$+ \frac{G_c}{l_0}\int_\Omega \left(d\,\delta d + l_0^2\, \nabla d\, \nabla\delta d\right)d\Omega, \tag{7}$$

which is the variational form that we solve numerically. Integration by parts gives

$$\partial_d\Pi^{ii}(\mathbf{u}, d)[\delta d] = \int_\Omega -2(1 - d)\psi_0^+(\varepsilon(\mathbf{u}))\delta d\, d\Omega$$
$$+ \frac{G_c}{l_0}\int_\Omega \left(d - l_0^2\, \nabla^2 d\right)\delta d\, d\Omega \tag{8}$$
$$+ G_c\, l_0 \int_{\partial\Omega_N} (\boldsymbol{\nabla} d \cdot \mathbf{n})\delta d\, d\partial\Omega.$$

Let us turn to the fourth-order formulation. In this case the variational form is

$$\partial_d \Pi^{iv}(\mathbf{u}, d)[\delta d] = \int_\Omega -2(1-d)\psi_0^+(\boldsymbol{\varepsilon}(\mathbf{u}))\delta d \, d\Omega$$
$$+ \frac{G_c}{l_0}\int_\Omega \left( d\,\delta d + \frac{l_0^2}{2}\,\nabla d\,\nabla\delta d + \frac{l_0^4}{16}\,\nabla^2 d\,\nabla^2\delta d \right)d\Omega, \tag{9}$$

which corresponds to the variational form that we solve numerically. Integrating by parts we get

$$\partial_d \Pi^{iv}(\mathbf{u}, d)[\delta d] = \int_\Omega -2(1-d)\psi_0^+(\boldsymbol{\varepsilon}(\mathbf{u}))\delta d \, d\Omega$$
$$+ \frac{G_c}{l_0}\int_\Omega \left( d - \frac{l_0^2}{2}\,\nabla^2 d + \frac{l_0^4}{16}\,\nabla^4 d \right)\delta d \, d\Omega$$
$$+ \frac{G_c\, l_0}{2}\int_{\partial\Omega}\left(\left(\left(\boldsymbol{\nabla} d - \frac{l_0^2}{8}\,\boldsymbol{\nabla}(\nabla^2 d)\right)\cdot \mathbf{n}\right)\right.$$
$$\left.\delta d + \frac{l_0^2}{8}\,\nabla^2 d(\boldsymbol{\nabla}\delta d \cdot \mathbf{n})\right)d\partial\Omega. \tag{10}$$

## 3 Numerical discretization strategy

Due to the irreversibility of the fracture phenomenon, the problem is path dependent and its solution requires a time integration of the mechanical model enforcing irreversibility in time.

### 3.1 Time discretization

First, let us consider a discretization of the time interval. Given $\mathbf{u}_{n-1}$ and $d_{n-1}$ at time $t_{n-1}$, we seek $\mathbf{u}_n$ and $d_n$, such that

$$\begin{cases} \partial_{\mathbf{u}} \Pi^{ii,iv}(\mathbf{u}_n, d_n) = \mathbf{0}, \\ \partial_d \Pi^{ii,iv}(\mathbf{u}_n, d_n) \geq 0, \\ \partial_d \Pi^{ii,iv}(\mathbf{u}_n, d_n)[d_n - d_{n-1}] = 0, \quad d_n \geq d_{n-1}. \end{cases} \tag{11}$$

Introducing the increment $\Delta d$ as independent variable, we get the variational inequality:

$$\begin{cases} \partial_d \Pi^{ii,iv}(\mathbf{u}_n, d_{n-1} + \Delta d_n) \geq 0, \\ \partial_d \Pi^{ii,iv}(\mathbf{u}_n, d_{n-1} + \Delta d_n)[\Delta d_n] = 0, \quad \Delta d_n \geq 0. \end{cases} \tag{12}$$

By linearity of $\partial_d \Pi^{ii,iv}$ with respect to $\Delta d$, we can further write

$$\begin{cases} \partial_d \Pi^{ii,iv}(\mathbf{u}_n, \Delta d_n) + \partial_d \Pi^{ii,iv}(\mathbf{u}_n, d_{n-1}) \geq 0, \\ (\partial_d \Pi^{ii,iv}(\mathbf{u}_n, \Delta d_n) + \partial_d \Pi^{ii,iv}(\mathbf{u}_n, d_{n-1}))[\Delta d_n] = 0, \quad \Delta d_n \geq 0. \end{cases}$$
$$\tag{12 bis}$$

which will be the linear complementary problem to be solved numerically, see (18).

System (11) is conveniently solved in a staggered manner, namely considering sequences of minimization problems, such that the energy of the system is alternatively minimized with respect to the displacement and the phase-field variable. First of all, we define the solution spaces $\mathcal{U}_{\mathbf{u}}$ and $\mathcal{U}_d^{ii,iv}$:

$$\mathcal{U}_{\mathbf{u}} := \{\mathbf{u}_n \in H^1(\Omega;\mathbb{R}^N) : \mathbf{u}_n = \bar{\mathbf{u}}_n \text{ on } \partial\Omega_D\},$$

and

$$\mathcal{U}_d^{ii} := \{d_n \in H^1(\Omega) : d_n \geq d_{n-1}\}$$
$$\mathcal{U}_d^{iv} := \{d_n \in H^2(\Omega) : d_n \geq d_{n-1}\}.$$

Therefore, we introduce the auxiliary sequences $\mathbf{u}^i$ and $d^i$ defined recursively by the following staggered scheme: [3]:

$$\begin{cases} \mathbf{u}^i \in \text{argmin}\{\Pi^{ii,iv}(\mathbf{u}^i, d^{i-1}) : \mathbf{u}^i \in \mathcal{U}_{\mathbf{u}}, \}, \\ d^i \in \text{argmin}\{\Pi^{ii,iv}(\mathbf{u}^i, d^i) : d^i \in \mathcal{U}_d^{ii,iv} \text{ with } d^i \geq d_{n-1}\}, \end{cases} \tag{13}$$

where $i = 1, 2, .., m$ is the $i$-th staggered iteration up to convergence, and then we set $\mathbf{u}_n = \mathbf{u}^m$ and $d_n = d^m$. Further details on the staggered scheme are given in Appendix C.

### 3.2 Spatial discretization with a focus on the the phase-field problem

For simplicity of notation, we disregard both the time variable and the staggered iteration index (i.e., we drop subscripts $(.)_n$ or superscripts $(.)^i$), thereby focusing our discussion on the spatial discretization. Adopting the Galerkin approach, we consider the approximate solution spaces $\mathcal{U}_{\mathbf{u}}^h \subseteq \mathcal{U}_{\mathbf{u}}$ and $\mathcal{U}_d^h \subseteq \mathcal{U}_d^{ii,iv}$ and the approximate trial spaces $\mathcal{V}_{\delta\mathbf{u}}^h \subseteq \mathcal{V}_{\delta\mathbf{u}}$ ($\mathcal{V}_{\delta\mathbf{u}} := \{\delta\mathbf{u}_n \in H^1(\Omega;\mathbb{R}^{n_d}) : \delta\mathbf{u}_n = \mathbf{0} \text{ on } \partial\Omega_D\}$) and ($\mathcal{V}_{\delta d}^{ii,iv})^h \subseteq \mathcal{V}_{\delta d}^{ii,iv}$ ($\mathcal{V}_d^{ii} := \{\delta d_n \in H^1(\Omega) : \delta d_n \geq \delta d_{n-1}\}$, $\mathcal{V}_d^{iv} := \{\delta d_n \in H^2(\Omega) : \delta d_n \geq \delta d_{n-1}\}$).

While the solution of the balance of linear momentum equation (6) for both the investigated phase-field formulations requires $H^1$-minimum regularity, the discretization of the variational inequality (12) demands basis functions with different minimum continuity requirements, namely $H^1$ for the second-order formulation and $H^2$ for the fourth-order one. Thus, given these high-order continuity requirements, IgA represents a natural modeling framework to compare the considered formulations. To this end, we consider the same dicretization choice, namely quadratic $C^1$-continuous B-splines or non-uniform rational B-splines (NURBS) for both second-order and fourth-order phase-field approaches.

### 3.2.1 Bivariate NURBS discretization

Without loss of generality, we restrict our attention to bivariate NURBS as all results provided in the numerical section comprise plane strain examples. For more details on the construction and properties of these functions, we refer interested readers to [12, 19, 20] and references therein.

The physical domain $\Omega \subset \mathbb{R}^2$ is the image of the parametric domain $\tilde{\Omega} = [0\ 1]^2$ through the mapping $F : \xi \in \tilde{\Omega} \to x \in \Omega$, such that every point $\xi = (\xi^1, \xi^2)$ is mapped onto its physical image $x$. Then, to characterize IgA multivariate shape functions, we introduce a compact notation, such that the vector-index $\mathbf{i} = \{i_1, i_2\}$ describes the actual position of the bivariate basis function in the tensor-product structure and $\mathbf{p} = \{p_1, p_2\}$ is the vector of polynomial degrees. Therefore, bidimensional geometries $\mathbf{S}(\xi)$ are constructed combining bivariate NURBS basis functions $R_{\mathbf{i},\mathbf{p}}$ with the control point vector $\hat{\mathbf{P}}_{\mathbf{i}}$ and read

$$\mathbf{S}(\xi) = \sum_{\mathbf{i}} R_{\mathbf{i},\mathbf{p}}(\xi)\hat{\mathbf{P}}_{\mathbf{i}}. \tag{14}$$

Consequently, starting from Eq. (14) we proceed to introduce the approximate global displacement $\mathbf{u}_\mathrm{h}$ and phase-field variable $\mathrm{d}_\mathrm{h}$, as well as the virtual displacements $\delta\mathbf{u}_\mathrm{h}$ and phase field $\delta\mathrm{d}_\mathrm{h}$ as

$$\mathbf{u} \approx \mathbf{u}_\mathrm{h} = \sum_{\mathbf{i}} \mathbf{R}_{\mathbf{i},\mathbf{p}}^{\mathbf{u}}\, \hat{\mathbf{u}}_{\mathbf{i}}, \qquad \delta\mathbf{u} \approx \delta\mathbf{u}_\mathrm{h} = \sum_{\mathbf{i}} \mathbf{R}_{\mathbf{i},\mathbf{p}}^{\mathbf{u}}\, \delta\hat{\mathbf{u}}_{\mathbf{i}},$$
$$\mathrm{d} \approx \mathrm{d}_\mathrm{h} = \sum_{\mathbf{i}} R_{\mathbf{i},\mathbf{p}}^{\mathrm{d}}\, \hat{\mathbf{d}}_{\mathbf{i}}, \qquad \delta\mathrm{d} \approx \delta\mathrm{d}_\mathrm{h} = \sum_{\mathbf{i}} R_{\mathbf{i},\mathbf{p}}^{\mathrm{d}}\, \delta\hat{\mathbf{d}}_{\mathbf{i}}, \tag{15}$$

where with superscripts $(.)^{\mathbf{u}}$ and $(.)^{\mathrm{d}}$ we highlight the displacement and phase-field discretizations, such that $R_{\mathbf{i},\mathbf{p}}^{\mathrm{d}} = R_{\mathbf{i},\mathbf{p}}$, while

$$\mathbf{R}_{\mathbf{i},\mathbf{p}}^{\mathbf{u}} = \begin{bmatrix} R_{\mathbf{i},\mathbf{p}} & 0 \\ 0 & R_{\mathbf{i},\mathbf{p}} \end{bmatrix}.$$

Then, as our aim is to provide an extensive comparison of the phase-field second- and fourth-order formulations described in Sect. 2, the two models differ only in the minimization of the fracture surface density functional (), while the displacement problem within a staggered iteration (11) is the same. Therefore, we focus our spatial discretization description on the phase-field problem only. To evaluate the positive part of the free energy density, we also introduce the approximate strain as

$$\varepsilon_\mathrm{h} = \sum_{\mathbf{i}} \mathbf{B}_{\mathbf{i},\mathbf{p}}^{\mathbf{u}}\, \hat{\mathbf{u}}_{\mathbf{i}}, \tag{16}$$

where, adopting Voigt's notation, $\mathbf{B}_{\mathbf{i},\mathbf{p}}^{\mathbf{u}}$ is the compatibility matrix defined as

$$\mathbf{B}_{\mathbf{i},\mathbf{p}}^{\mathbf{u}} = \begin{bmatrix} \frac{\partial R_{\mathbf{i},\mathbf{p}}}{\partial x_1} & 0 \\ 0 & \frac{\partial R_{\mathbf{i},\mathbf{p}}}{\partial x_2} \\ \frac{\partial R_{\mathbf{i},\mathbf{p}}}{\partial x_2} & \frac{\partial R_{\mathbf{i},\mathbf{p}}}{\partial x_1} \end{bmatrix}.$$

To treat the surface terms in Eqs. (7) and (9), we need to further detail the phase-field gradient and Laplacian approximations as well their virtual counterparts as

$$\nabla\mathrm{d} \approx \nabla\mathrm{d}_\mathrm{h} = \sum_{\mathbf{i}} \mathbf{B}_{\mathbf{i},\mathbf{p}}^{\mathrm{d}}\, \hat{\mathbf{d}}_{\mathbf{i}}, \qquad \nabla\delta\mathrm{d} \approx \nabla\delta\mathrm{d}_\mathrm{h} = \sum_{\mathbf{i}} \mathbf{B}_{\mathbf{i},\mathbf{p}}^{\mathrm{d}}\, \delta\hat{\mathbf{d}}_{\mathbf{i}},$$
$$\nabla^2\mathrm{d} \approx \nabla^2\mathrm{d}_\mathrm{h} = \sum_{\mathbf{i}} \mathbf{C}_{\mathbf{i},\mathbf{p}}^{\mathrm{d}}\, \hat{\mathbf{d}}_{\mathbf{i}}, \qquad \nabla^2\delta\mathrm{d} \approx \nabla^2\delta\mathrm{d}_\mathrm{h} = \sum_{\mathbf{i}} \mathbf{C}_{\mathbf{i},\mathbf{p}}^{\mathrm{d}}\, \delta\hat{\mathbf{d}}_{\mathbf{i}}, \tag{17}$$

where $\mathbf{B}_{\mathbf{i},\mathbf{p}}^{\mathrm{d}}$ is the matrix of the shape function derivatives

$$\mathbf{B}_{\mathbf{i},\mathbf{p}}^{\mathrm{d}} = \begin{bmatrix} \frac{\partial R_{\mathbf{i},\mathbf{p}}}{\partial x_1} & 0 \\ 0 & \frac{\partial R_{\mathbf{i},\mathbf{p}}}{\partial x_2} \end{bmatrix},$$

while $\mathbf{C}_{\mathbf{i},\mathbf{p}}^{\mathrm{d}}$ is the second-derivative shape functions vector that reads

$$\mathbf{C}_{\mathbf{i},\mathbf{p}}^{\mathrm{d}} = \left[ \frac{\partial^2 R_{\mathbf{i},\mathbf{p}}}{\partial x_1^2} + \frac{\partial^2 R_{\mathbf{i},\mathbf{p}}}{\partial x_2^2} \right].$$

## 3.3 Symmetric linear complementarity problem

In this work, we focus on the rigorous solution of the problem that arises from the constrained minimisation of the total energy with respect to the phase-field variable, which once spatially discretized turns into a Symmetric Linear Complementarity Problem (SLCP) that can be handled in a straightforward manner *via* the PSOR [21], also in the case of the considered high-order formulation. The irreversibility is enforced on the phase-field increment, and, therefore, we rewrite this relation highlighting its dependence upon $\Delta\mathrm{d}$ for a fixed staggered iteration $i$:

$$[\Delta\hat{\mathbf{d}}^i]^\mathrm{T}\, \partial_\mathrm{d}\Pi^{ii,iv}(\hat{\mathbf{u}}^i, \hat{\mathbf{d}}_{\mathrm{n}-1} + \Delta\hat{\mathbf{d}}^i)$$
$$= (\Delta\hat{\mathbf{d}}^i)^\mathrm{T} \overbrace{\left[ \mathbf{Q}_{ii,iv}^i(\hat{\mathbf{u}}^i, \hat{\mathbf{d}}_{\mathrm{n}-1})\Delta\hat{\mathbf{d}}^i + \mathbf{q}_{ii,iv}^i(\hat{\mathbf{u}}^i, \hat{\mathbf{d}}_{\mathrm{n}-1}) \right.}^{\partial_\mathrm{d}\Pi^{ii,iv}(\hat{\mathbf{u}}^i, \Delta\hat{\mathbf{d}}^i)}$$
$$\left. + \partial_\mathrm{d}\Pi^{ii,iv}(\hat{\mathbf{u}}^i, \hat{\mathbf{d}}_{\mathrm{n}-1}) \right]$$
$$= (\Delta\hat{\mathbf{d}}^i)^\mathrm{T} \left[ \mathbf{Q}_{ii,iv}^i(\hat{\mathbf{u}}^i, \hat{\mathbf{d}}_{\mathrm{n}-1})\Delta\hat{\mathbf{d}}^i + \tilde{\mathbf{q}}_{ii,iv}^i(\hat{\mathbf{u}}^i, \hat{\mathbf{d}}_{\mathrm{n}-1}) \right], \tag{18}$$

where the current phase-field solution at the control points is $\hat{\mathbf{d}}^i = \Delta\hat{\mathbf{d}}^i + \hat{\mathbf{d}}_{\mathrm{n}-1}$, the phase-field solution $\hat{\mathbf{d}}_{\mathrm{n}-1}$ is known from the previous step $\mathrm{n} - 1$, and the displacement $\hat{\mathbf{u}}^i$ is fixed. The

vector-quantity in the squared brackets is the sum of a linear term in $\Delta\hat{\mathbf{d}}^i$ (i.e., $\mathbf{Q}^i_{ii,iv}$ is constant) and a constant vector $\tilde{\mathbf{q}}^i_{ii,iv}$. In Eq. (18), the $ii, iv$-subscript denotes once again the matrix/vector discretized quantities $\mathbf{Q}^i_{ii,iv}$ and $\tilde{\mathbf{q}}^i_{ii,iv}$ that will be detailed below, according to the order of the adopted phase-field theory. The constitutive matrix $\mathbf{Q}^i_{ii,iv}$ and the vector $\tilde{\mathbf{q}}^i_{ii,iv}$ read, respectively

$$\mathbf{Q}^i_{ii,iv} := \mathbf{\Psi}(\hat{\mathbf{u}}^i) + G_c\,\mathbf{\Phi}_{ii,iv}, \quad \tilde{\mathbf{q}}^i_{ii,iv} := \mathbf{Q}^i_{ii,iv}\hat{\mathbf{d}}_n - \boldsymbol{\psi}(\hat{\mathbf{u}}^i), \quad (19)$$

where the free energy matrix $\mathbf{\Psi}$ and the vector $\boldsymbol{\psi}$, obtained from the spatial discretization of the elastic energy functional (2), are

$$\left(\mathbf{\Psi}(\hat{\mathbf{u}}^i)\right)_{\mathbf{ij}} := \int_\Omega 2\,\psi_0^+(\hat{\mathbf{u}}^i)\,R_{\mathbf{i,p}}\,R_{\mathbf{j,p}}\,\mathrm{d}\Omega,$$

$$\left(\boldsymbol{\psi}(\hat{\mathbf{u}}^i)\right)_{\mathbf{i}} := \int_\Omega 2\,\psi_0^+(\hat{\mathbf{u}}^i)\,R_{\mathbf{i,p}}\,\mathrm{d}\Omega. \quad (20)$$

The discretized positive part of the free energy density in (2) can be introduced as

$$\psi_0^+(\hat{\mathbf{u}}^i) = \frac{1}{2}\,\boldsymbol{\varepsilon}_h^{\mathrm{T}}\big(\mathrm{H}^+(\boldsymbol{\varepsilon}_h : \mathbf{I})K\,\mathbf{P}_v + \mu\,\mathbf{P}_d\big)\boldsymbol{\varepsilon}_h,$$

where $\mathbf{P}_v$ and $\mathbf{P}_d$ read, respectively:

$$\mathbf{P}_v = \begin{bmatrix} 1 & 1 & 0 \\ 1 & 1 & 0 \\ 0 & 0 & 0 \end{bmatrix}, \quad \mathbf{P}_d = \begin{bmatrix} 4/3 & -2/3 & 0 \\ -2/3 & 4/3 & 0 \\ 0 & 0 & 1 \end{bmatrix}, \quad (21)$$

while $\mathrm{H}^+(x) = \max(0, x)$ is the positive Heaviside function acting on the trace of the discretized strain tensor (16). The constant dissipation matrix $\mathbf{\Phi}_{ii,iv}$ in Eq. (19)$_1$ that is obtained from the spatial discretization of the phase-field energies (7), (9) is detailed according to the considered phase-field $ii, iv$-order theory as

$$\left(\mathbf{\Phi}_{ii}\right)_{\mathbf{ij}} := \int_\Omega \left(l_0^{-1} R_{\mathbf{i,p}} R_{\mathbf{j,p}} + l_0\,\mathbf{B}_{\mathbf{i,p}}^{\mathrm{d}}\,\mathbf{B}_{\mathbf{j,p}}^{\mathrm{d}}\right)\mathrm{d}\Omega,$$

$$\left(\mathbf{\Phi}_{iv}\right)_{\mathbf{ij}} := \int_\Omega \left(l_0^{-1} R_{\mathbf{i,p}} R_{\mathbf{j,p}} + \frac{l_0}{2}\,\mathbf{B}_{\mathbf{i,p}}^{\mathrm{d}}\,\mathbf{B}_{\mathbf{j,p}}^{\mathrm{d}} + \frac{l_0^3}{16}\,\mathbf{C}_{\mathbf{i,p}}^{\mathrm{d}}\,\mathbf{C}_{\mathbf{j,p}}^{\mathrm{d}}\right)\mathrm{d}\Omega. \quad (22)$$

Then, regardless the order of the considered theory the rigorous solution of the constrained phase-field problem turns to be equivalent to the SLCP:

$$\begin{cases} (\Delta\hat{\mathbf{d}}^i)^{\mathrm{T}}\left(\mathbf{Q}^i_{ii,iv}\Delta\hat{\mathbf{d}}^i + \tilde{\mathbf{q}}^i_{ii,iv}\right) = 0 \\ \left(\mathbf{Q}^i_{ii,iv}\Delta\hat{\mathbf{d}}^i + \tilde{\mathbf{q}}^i_{ii,iv}\right) \geq \mathbf{0}, \quad \Delta\hat{\mathbf{d}}^i \geq \mathbf{0}, \end{cases} \quad (23)$$

where the first equality, i.e., the complementarity condition, defines the discretized form of the phase-field activation condition, the first inequality defines the region of linear elastic regime, and the second inequality enforces the irreversibility condition [8].

# 4 Numerical results

The aim of this section is to provide an exhaustive comparison in terms of accuracy between the considered second- and fourth-order models. To this end, we first study two tests providing a straight-line fracture pattern (hereafter referred to as "simple" crack pattern): the double cantilever beam (DCB) [10, 16] and the single edge notched (SEN) tensile test [6]. To carry out an in-depth study of the accuracy, as in [10], tests with more complex crack patterns and geometries are also considered, i.e., the SEN shear test [9, 16], the asymmetric double pre-notch [22], and the quarter of annulus. Following [10], the accuracy evaluation is based on an estimate of the fracture length, which we compute using an image-based algorithm (see Appendix B) that we test for progressively more complex crack patterns. Given the evolutionary nature of the phase-field problem, particular attention is devoted to the imposition of the initial crack-field condition. Specifically, we represent this physical discontinuity with an initial pre-field, that we compare with a state of the art method, such as the $\mathcal{H}_0$ method proposed in [9]. In Appendix A, we investigate the role of the phase-field initial condition at the control points or of the interpolated phase-field (IPF) variable approach, which we test against a well established literature benchmark, i.e., the centre-cracked plate test [23].

## 4.1 Double cantilever beam

The double cantilever beam test is often used to study accuracy [10]. The specimen is characterized by a square geometry of side equal to 1 mm, internal length $l_0 = 0.015$ mm, material toughness $G_c = 0.01$ kN/mm, and Young Modulus and Poisson's ratio $E = 100$ kN/mm$^2$ and $\nu = 0.25$, respectively. A quasi-static displacement-controlled loading history is considered, characterized by 7 loading steps: starting from $u_0 = 0.01$ mm, we use an increment $\Delta u = 5 \cdot 10^{-3}$ mm up to the maximum displacement $u_{max} = 0.04$ mm. A $7.5 \cdot 10^{-3}$ mm pre-field is imposed with the $\mathcal{H}_0$ method, while geometry and boundary conditions are summarized in Fig. 2.

To compare the accuracy between the second- and fourth-order models we consider several uniform meshes of mesh-size determined as a function of the internal
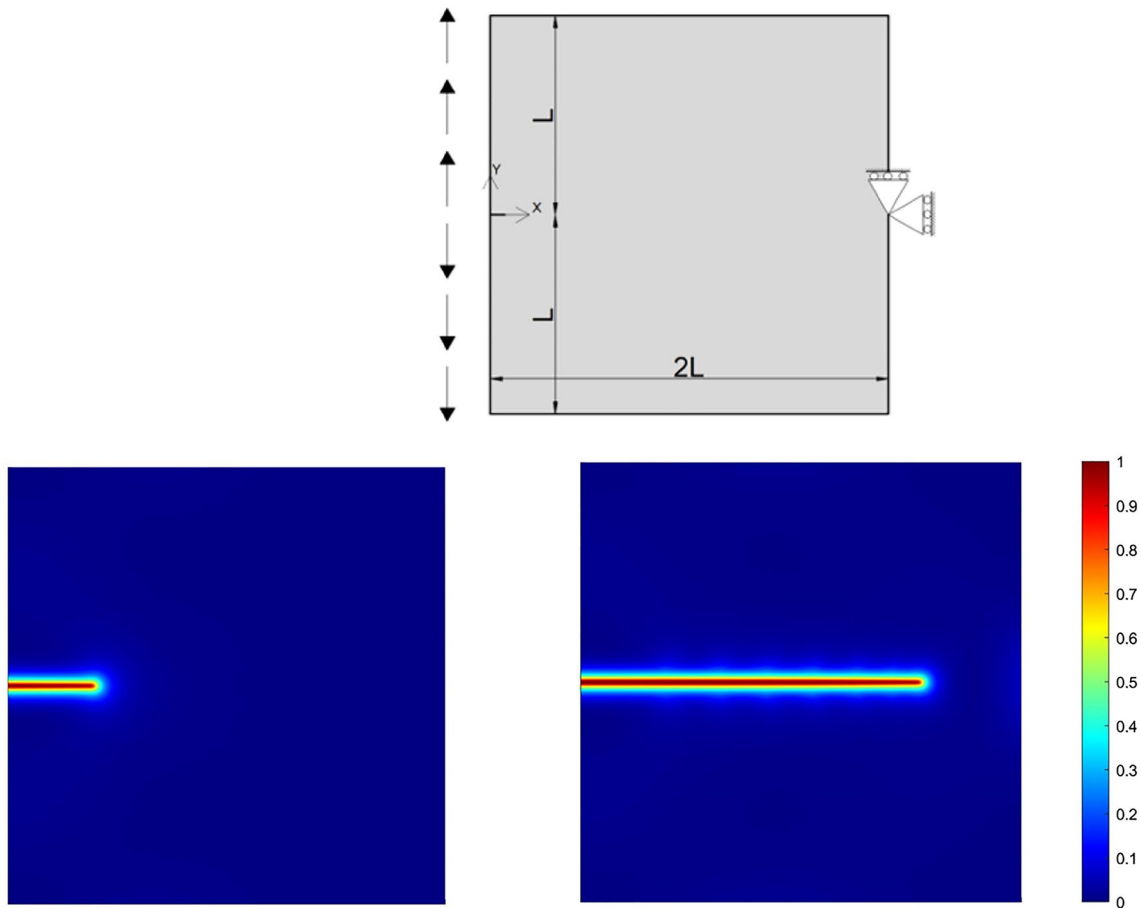
**Fig. 2** Top row: geometry and boundary conditions for the DCB test. Bottom row: from left to right, first and last loading step crack pattern, respectively, for the second-order functional considering $h = l_0/4$

length $l_0$, namely $h = \{l_0, l_0/2, l_0/4, l_0/6\}$. More details on mesh-relevant quantities are summarized in Tab. 1. All analyses are performed with quadratic shape functions with $C^1$-continuity.

Following [10], for each mesh, the change in dissipated energy $\Delta\mathcal{D}$ and the change in crack length $\Delta a$ between the loading steps i and j is computed. The effective toughness is evaluated as

$$G_c^{Eff} = \frac{\Delta\mathcal{D}}{\Delta a} = \frac{\mathcal{D}_j - \mathcal{D}_i}{a_j - a_i}. \tag{24}$$

**Table 1** Mesh features

| $h$ | Elements | Control points |
|---|---|---|
| [mm] | (–) | (–) |
| $l_0$ | 4624 | 4900 |
| $l_0/2$ | 18,496 | 19,044 |
| $l_0/4$ | 72,900 | 73,984 |
| $l_0/6$ | 160,000 | 161,604 |

For this test, the differences $\Delta\mathcal{D}$ and $\Delta a$ are evaluated by taking into account the first and last loading steps: i = 1 and j = 7. Then, to assess the accuracy, the relative error on the toughness is computed as

$$\text{Error} = \frac{G_c^{Eff} - G_c}{G_c} = \frac{\Delta G_c^{Eff}}{G_c}. \tag{25}$$

All results related to the error evaluations for this test are summarized in Tables 2 and 3, whereas Fig. 3 shows the accuracy trend for the second- and fourth-order functionals. It can be observed that the fourth-order model is always more accurate than the second-order one when comparing the two problems with the same mesh size. Moreover, it can be observed that the second- and fourth-order models have comparable accuracy when the latter formulation comprises a mesh-size two times larger.

More specifically, the second-order formulation with four elements in the internal length and the fourth-order one with two elements showcase a comparable relative toughness error (see Tables 2-3). This allows us to compare the two methods

**Table 2** DCB test: second-order model accuracy evaluation

| $h$ | $a_0$ | $\Delta a$ | $G_c^{Eff}$ | $\Delta G_c^{Eff}$ | Conv. rate | Error |
|---|---|---|---|---|---|---|
| [mm] | [mm] | [mm] | [kN/mm] | [kN/mm] | [–] | [%] |
| $l_0$ | 0.1397 | 0.5000 | 0.0183 | 0.0083 | – | 82.9 |
| $l_0/2$ | 0.1654 | 0.5441 | 0.0145 | 0.0045 | 0.883 | 45.1 |
| $l_0/4$ | 0.1833 | 0.5704 | 0.0123 | 0.0023 | 0.968 | 23.2 |
| $l_0/6$ | 0.1922 | 0.5750 | 0.0116 | 0.0016 | 0.895 | 16.4 |

**Table 3** DCB test: fourth-order model accuracy evaluation

| $h$ | $a_0$ | $\Delta a$ | $G_c^{Eff}$ | $\Delta G_c^{Eff}$ | Conv. rate | Error |
|---|---|---|---|---|---|---|
| [mm] | [mm] | [mm] | [kN/mm] | [kN/mm] | [–] | [%] |
| $l_0$ | 0.1544 | 0.5000 | 0.0175 | 0.0075 | – | 74.6 |
| $l_0/2$ | 0.1801 | 0.5588 | 0.0129 | 0.0029 | 1.371 | 28.9 |
| $l_0/4$ | 0.1944 | 0.5778 | 0.0110 | 0.0010 | 1.536 | 10.1 |
| $l_0/6$ | 0.1987 | 0.5800 | 0.0105 | 0.0005 | 1.709 | 5.42 |
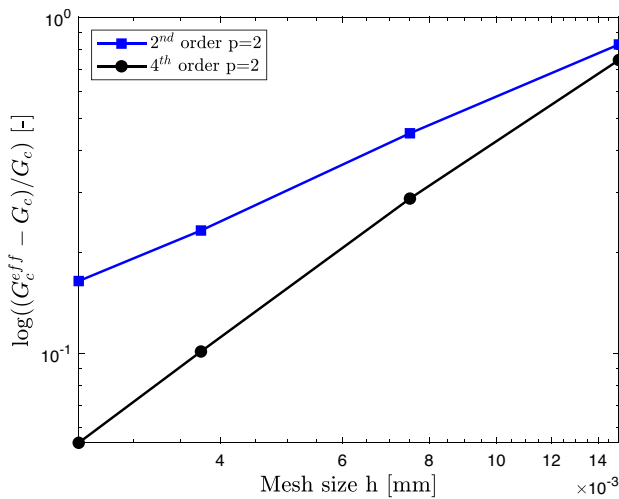


**Fig. 3** DCB test. Comparison of accuracy at different mesh sizes

for the same accuracy and appreciate a substantial reduction of the total computational time guaranteed by the fourth-order model. In fact, for the second-order functional with $h = l_0/4$, the elapsed time for the analysis is 20 h 20 min against the fourth-order one with $h = l_0/2$ that completes the analysis in 3 h 32 min, which corresponds to a 80–85% time saving[1] and a 30% saving in the number of iterations. In Tabs. 2 and 3, we also evaluate the convergence rate [10] as

$$\text{Conv. rate} = \frac{\log\left((\Delta G_c^{eff})_{k+1}\right) - \log\left((\Delta G_c^{eff})_k\right)}{\log\left(h_{k+1}\right) - \log\left(h_k\right)}, \qquad (26)$$

where, with two subsequent meshes $h_k$ and $h_{k+1}$, we consider the corresponding absolute errors $\log\left((\Delta G_c^{eff})_k\right)$ and $\log\left((\Delta G_c^{eff})_{k+1}\right)$, respectively, that are computed as the difference between the effective toughness and the material toughness (24) (i.e., $\Delta G_c^{Eff} = G_c^{Eff} - G_c$). From Tabs. 2–3 it can be seen that for this test the fourth-order model converges nearly two times faster than the second-order one.

## 4.2 SEN tensile test

In the SEN tensile test, the specimen presents a square geometry with a side of 1 mm. The considered material properties are: internal length $l_0 = 0.015$ mm, material toughness $G_c = 2.7 \cdot 10^{-3}$ kN/mm, Young modulus $E = 210$ kN/mm$^2$, and Poisson ratio $\nu = 0.3$. The displacement-based loading history is characterized by a maximum displacement $u_{max} = 6 \cdot 10^{-3}$ mm with a steady increment $\Delta u = 3 \cdot 10^{-4}$ mm. This test considers a pre-crack of length equal to half the specimen side and is modeled by a pre-field imposed as an IPF as described in Appendix A. The load and boundary conditions are summarized in Fig. 4. In this study, two different mesh sizes are considered: $h = l_0/2$ corresponding to 18,496 elements and 19,044 control points, and $h = l_0/4$ corresponding to 72,900 elements and 73,984 control points. The analyses are performed with quadratic shape functions with $C^1$-continuity. The tests compare accuracy, cumulative computational time, and peak reactions of the considered second- and fourth-order formulations. As it can be seen in Fig. 5, the main difference from the DCB test is that in this case the final fracture length is equal to the side of the sample. This allows to have a reference value in the accuracy analysis, since the developed fracture length is always half of the sample side. As for the DCB test, the variation of fracture
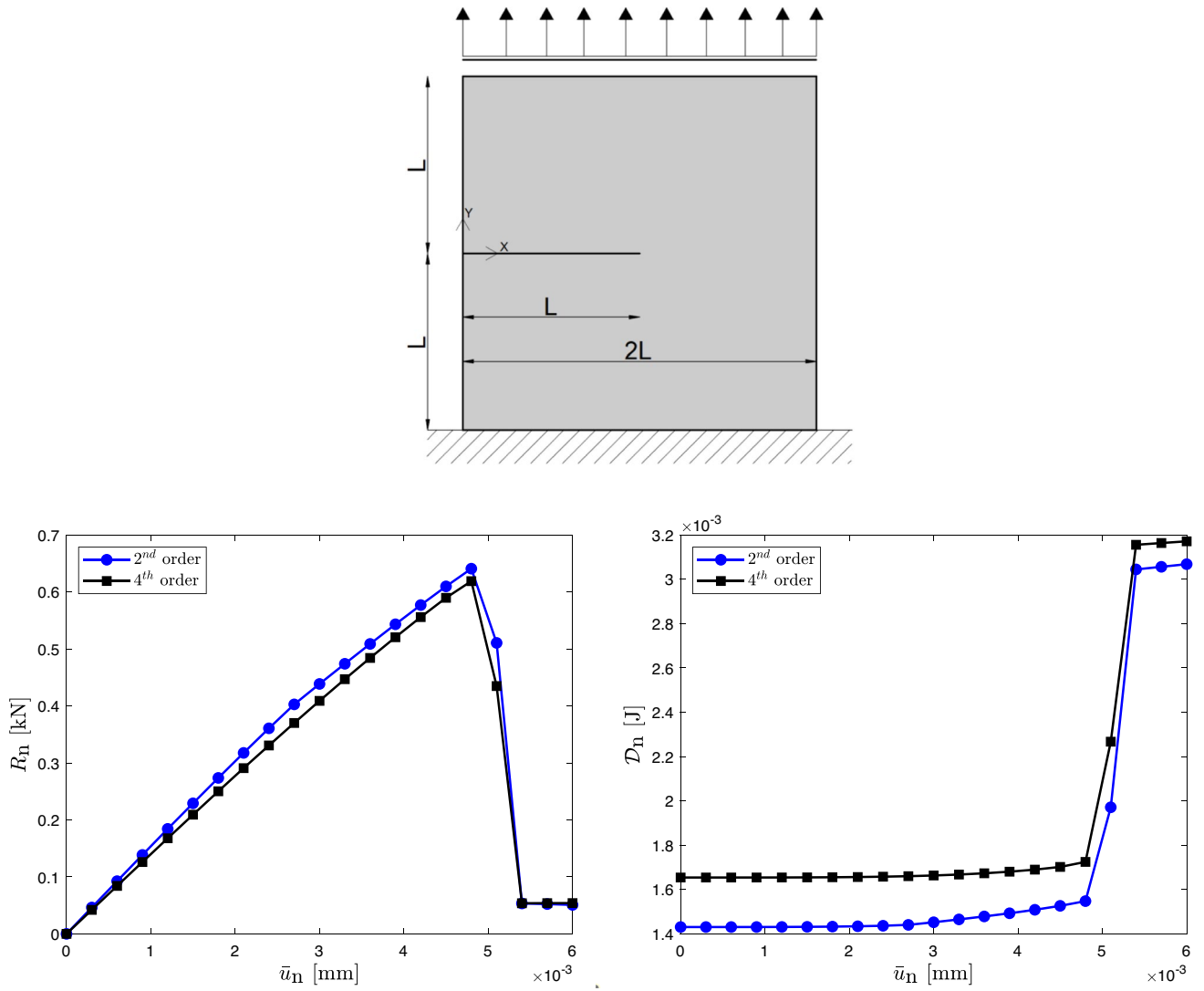
---

[1] All tests were run on a PC with an Intel CORE i7 11th generation processor, 24 GB RAM, Windows 10.

**Fig. 4** SEN tensile test. Top row: geometry and boundary conditions. Bottom row: from left to right, reaction and dissipated energy curves obtained comparing the second-order formulation using $h = l_0/4$ and the fourth-order one with $h = l_0/2$
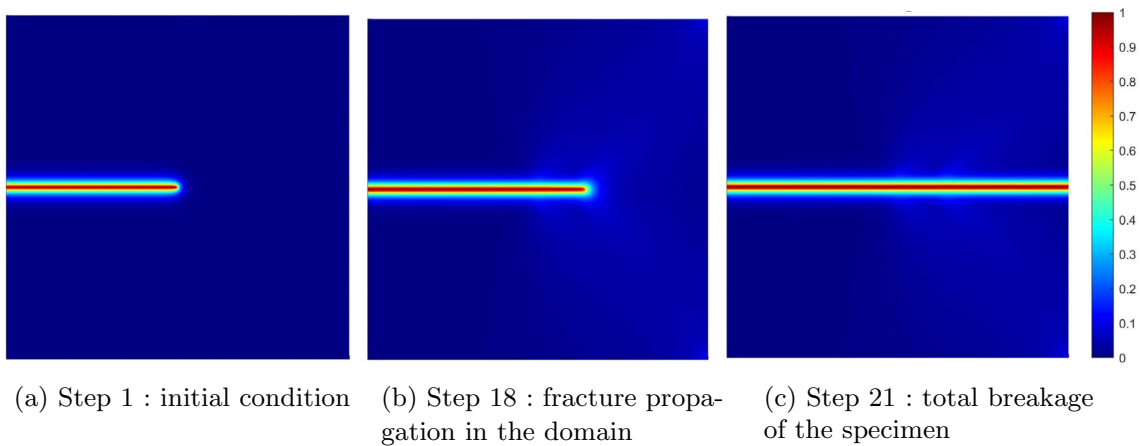


(a) Step 1 : initial condition

(b) Step 18 : fracture propagation in the domain

(c) Step 21 : total breakage of the specimen

**Fig. 5** SEN tensile test. Crack pattern of three different loading steps for the second-order functional considering $h = l_0/4$

**Table 4** SEN tensile test: second-order model accuracy evaluation

| $h$ | $G_c^{Eff}$ | $\Delta G_c^{Eff}$ | Conv. rate | Error | $R_n$ | Time spent |
|---|---|---|---|---|---|---|
| [mm] | [kN/mm] | [kN/mm] | [-] | [%] | [kN] | [h:min] |
| $l_0/2$ | $3.395 \cdot 10^{-3}$ | $6.947 \cdot 10^{-4}$ | - | 25.7 | 0.652 | 08:45 |
| $l_0/4$ | $3.275 \cdot 10^{-3}$ | $5.749 \cdot 10^{-4}$ | 0.273 | 21.3 | 0.640 | 33:41 |

**Table 5** SEN tensile test: fourth-order model accuracy evaluation

| $h$ | $G_c^{Eff}$ | $\Delta G_c^{Eff}$ | Conv. rate | Error | $R_n$ | Time spent |
|---|---|---|---|---|---|---|
| [mm] | [kN/mm] | [kN/mm] | [-] | [%] | [kN] | [h:min] |
| $l_0/2$ | $3.034 \cdot 10^{-3}$ | $3.341 \cdot 10^{-4}$ | – | 12.4 | 0.622 | 07:45 |
| $l_0/4$ | $2.914 \cdot 10^{-3}$ | $2.139 \cdot 10^{-4}$ | 0.643 | 7.90 | 0.593 | 24:10 |

length and dissipated energy are evaluated between the first and the last loading steps, and the fourth-order model is always more accurate than the second-order one. The results in Tables 4 and 5 allow us to compare the two models for different mesh sizes. If we compare the fourth-order with $h = l_0/2$ and the second-order with $h = l_0/4$, we notice that the fourth-order is more accurate than the second-one and the peak reactions are comparable (see Fig. 4). In terms of total time required by the analysis, the fourth-order model considering $h = l_0/2$ is more than four times faster than the second-order one with $h = l_0/4$. Moreover, the convergence rate of the fourth-order functional is for this test approximately three times greater than that of the second-order one.

### 4.3 SEN shear test

The accuracy study proposed in [10] considers tests with linear crack patterns only. In order to provide a comprehensive comparison of the considered models we turn our attention to the SEN shear test [7, 9, 16] which provides a more challenging crack pattern evolution (see Fig. 7).

The challenge in this case is the measurement of the crack length, which we propose to carry out by an image-based algorithm, as detailed in Appendix B. The sample considered in this test presents a square geometry with a side of 1 mm and the material properties are: internal length $l_0 = 0.01$ mm, material toughness $G_c = 2.7 \cdot 10^{-3}$ kN/mm, Young modulus $E = 210$ kN/mm$^2$, and Poisson ration $\nu = 0.3$. A quasi-static displacement-control loading history is applied. It consists of 21 loading steps, with a minimum displacement $u_{min} = 6 \cdot 10^{-3}$mm, a steady increment $\Delta u = 3 \cdot 10^{-4}$ mm and a maximum displacement $u_{max} = 12 \cdot 10^{-3}$ mm. The initial pre-crack is located at $y = 0$ and $x \in [0, 0.5]$ mm and is modeled with the technique of the interpolated phase-field variable pre-crack imposition (see Appendix A). The loading and boundary conditions are summarized in Fig. 6 (top row).

As for the SEN tensile test, two different mesh sizes are considered: $h = l_0/2$ with 40,401 elements and 41,209 control points and $h = l_0/4$ with 160,801 elements and 162,409 control points. Quadratic shape functions of $C^1$-continuity are used.

As already mentioned, for this test with a non straight crack pattern, the measurement of the crack length is not trivial. To do that, we use the imaged-based algorithm (see Appendix B) that allows us to easily track the curved crack pattern and, hence, to calculate the effective toughness and assess its accuracy. The effectiveness of the algorithm has been first validated by considering simple geometric figures whose *a priori* lengths are known, such as: a circle of unit radius, a horizontal segment, and a segment inclined of $\pi$/4. For all cases, a good estimate of the object length was obtained. The results of the SEN shear test are summarized in Tables 6–7.

In addition, in this case, it can be observed that the fourth-order functional considering $h = l_0/2$ showcases a relative error in term of $G_c$ comparable to the second-order functional with $h = l_0/4$. Another consideration concerns the peak reaction: it can be seen in Fig. 6 that the second-order formulation with the finest mesh and the fourth-order one considering the coarsest mesh have the same peak value. Moreover the fourth-order case presents a rate of convergence that is twice the one provided by the second-order formulation. Furthermore, the fourth-order formulation allows for a four time faster analysis in terms of computational time and for a 30% reduction of the number of iterations.

### 4.4 Quarter of annulus test

In this section, we study the accuracy of the analysis of a quarter of annulus. This provides a good test to compare the considered second- and fourth-order formulations in the case of a non-trivial geometry. The internal length is $l_0 = 0.02$ mm, the toughness $G_c = 2.7 \cdot 10^{-3}$ kN/mm, the Young modulus $E = 210$ kN/mm$^2$, and the Poisson ratio $\nu = 0.3$. The sample features an internal radius $R_i = 1$ mm and an external radius $R_e = 2$ mm and considers simply supported constraints, positioned at $x \in [R_i, R_e]$, $y = 0$
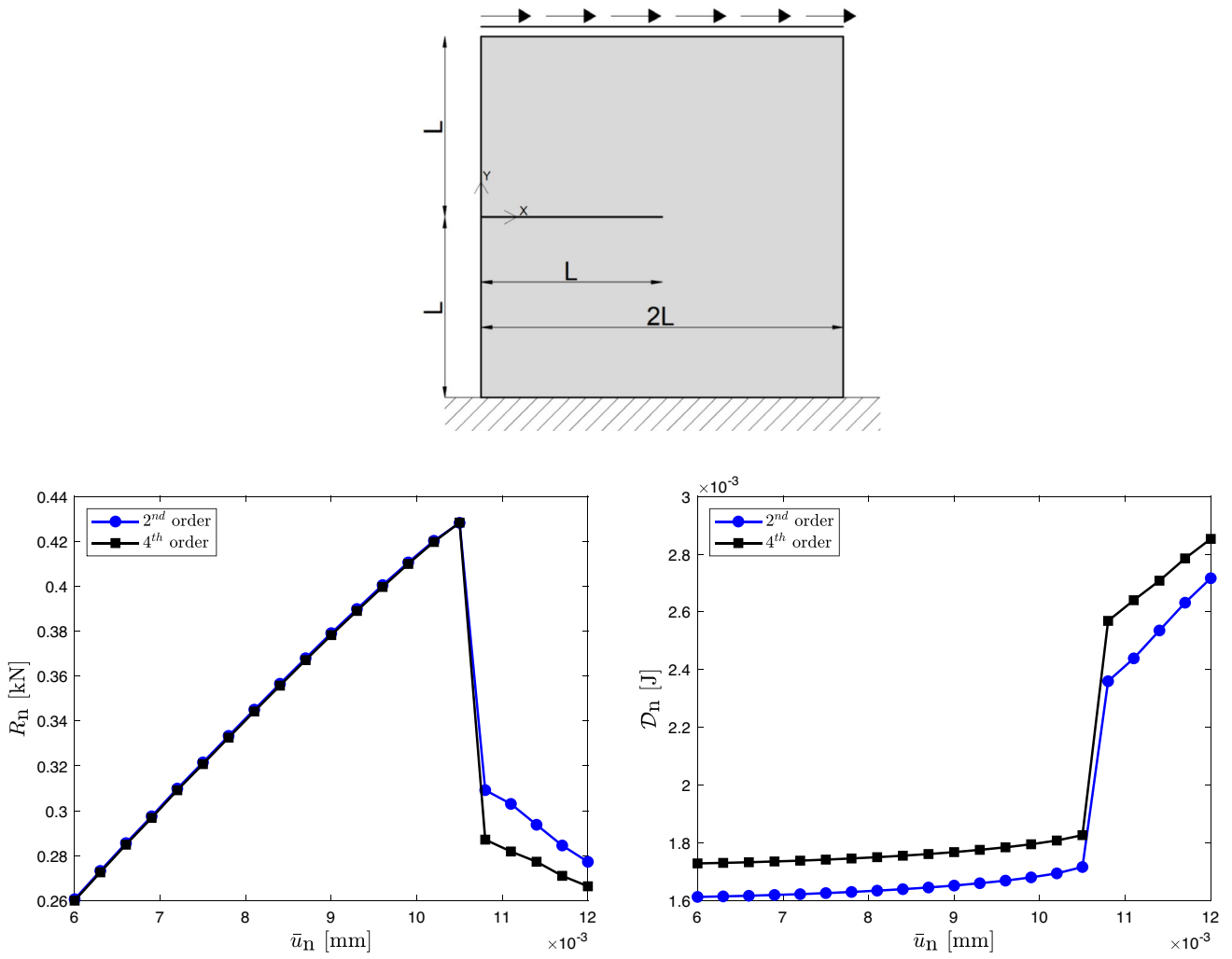
**Fig. 6** SEN shear test. Top row: geometry and boundary conditions. Bottom row: from left to right, reaction and dissipated energy curves obtained comparing the second-order formulation using $h = l_0/4$ and the fourth-order one with $h = l_0/2$
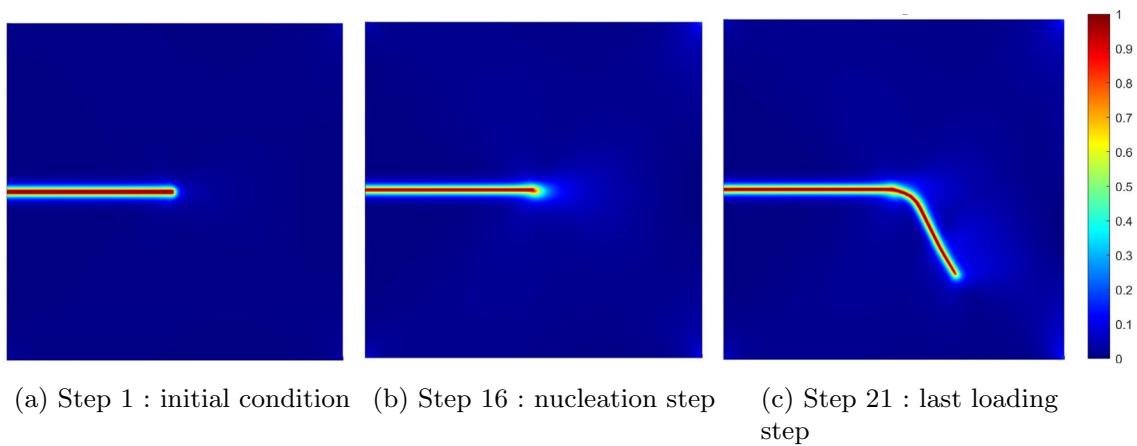


(a) Step 1 : initial condition    (b) Step 16 : nucleation step    (c) Step 21 : last loading step

**Fig. 7** SEN shear test. Crack pattern for three different loading steps for second-order functional considering $h = l_0/4$

**Table 6** SEN shear test: second-order model accuracy evaluation

| $h$ | $\Delta a$ | $G_c^{Eff}$ | $\Delta G_c^{Eff}$ | Conv. rate | Error | $R_n$ | Time spent |
|---|---|---|---|---|---|---|---|
| [mm] | [mm] | [kN/mm] | [kN/mm] | [-] | [%] | [kN] | [h:min] |
| $l_0/2$ | $2.731 \cdot 10^{-1}$ | $4.043 \cdot 10^{-3}$ | $1.343 \cdot 10^{-4}$ | – | 49.5 | 0.499 | 11:52 |
| $l_0/4$ | $3.011 \cdot 10^{-1}$ | $3.666 \cdot 10^{-3}$ | $9.664 \cdot 10^{-4}$ | 0.475 | 35.8 | 0.428 | 63:19 |

**Table 7** SEN shear test: fourth-order model accuracy evaluation

| $h$ | $\Delta a$ | $G_c^{Eff}$ | $\Delta G_c^{Eff}$ | Conv. rate | Error | $R_n$ | Time spent |
|---|---|---|---|---|---|---|---|
| [mm] | [mm] | [kN/mm] | [kN/mm] | [-] | [%] | [kN] | [h:min] |
| $l_0/2$ | $3.142 \cdot 10^{-1}$ | $3.578 \cdot 10^{-3}$ | $8.781 \cdot 10^{-4}$ | – | 32.5 | 0.428 | 16:28 |
| $l_0/4$ | $3.571 \cdot 10^{-1}$ | $3.191 \cdot 10^{-3}$ | $4.908 \cdot 10^{-4}$ | 0.839 | 18.2 | 0.406 | 74:47 |

and $x = 0$, $y \in [R_i, R_e]$. We impose a quasi-static displacement-based loading history that applies one shear load at $x \in [R_i, R_e]$, $y = 0$, in the direction of positive $x$ and the other one at $x = 0$, $y \in [R_i, R_e]$, in the direction of positive $y$. The loading history consists of 20 loading steps, with a steady increment $\Delta u = 10^{-3}$ mm and a maximum displacement $u_{max} = 1.9 \cdot 10^{-2}$ mm. A pre-field phase-field point is imposed along the $\pi/4$ inclined radius of the specimen using the $\mathcal{H}_0$ method [9].

The load setting and boundary conditions are summarized in Fig. 8, while the mesh is uniform over the body domain and in this study we consider four different mesh sizes as summarized in detail in Table 8.

To compute the effective toughness (24), we take into account the nucleation step and the step corresponding to the complete specimen rupture. Consequently, also in this case the fracture length coincides with the difference between the internal and external radii (see Fig. 9) as our geometry, boundary, and loading conditions are symmetric. We also highlight in Fig. 9 that the cracks obtained with a fourth-order formulation are wider than in the case of the second-order model because the comparison is made with different meshes: for the second-order, we use 4 elements to resolve the parameter $l_0$ (namely we consider the classical rule of thumb present in the literature), whereas for the fourth-order model 2 elements are considered, resulting in a comparable level of accuracy but in a wider crack.

From Tables 9 and 10 it can be observed that also in this case the fourth-order model is more accurate than the second-order one for the same mesh-size. It can be observed in Fig. 10 that the fourth-order model with mesh-size $h = l_0/4$ showcases a comparable accuracy with respect to the second-order model with mesh $h = l_0/8$ and for both tests the peak reactions are similar. If we compare the total elapsed times (normalized with respect to the analysis time of the corresponding second-order model, that features $h = l_0/8$), we observe that the fourth-order model allows to save $\sim 83$ % of the required computational time with respect to the second-order one.

In addition, for this test, we have that for the same mesh the fourth-order model is always more accurate than the second-order one and that the two models show comparable accuracy with meshes twice as coarse, for the fourth-order model, with significant savings in computational time, memory, and engineering quantities of interest, such as peak reactions.

**Remark:** If the pre-field is not introduced, the fracture nucleates along the constrained boundary. Then, two important considerations follow: (i) due to the symmetry conditions, it is more convenient for phase field to nucleate at the boundary, (ii) the fracture energy at the edge is relative to the detachment of the constrained boundary from the domain, so that a different $G_c$ between the domain and the fixed edge should be considered. Another possible way to force the phase field to propagate inside the domain (and not along the constrained boundary) is to insert a band of width $l_0$ in which we impose that the phase field is zero. This is equivalent to imposing that the material is not damaged along the constrained edge.

### 4.5 Asymmetric double pre-notch test

This benchmark considered in [22] is more challenging because the crack pattern is characterized by two fractures that do not touch each other due to the occurrence of coalescence phenomena. The sample features a square geometry with a side of 1 mm. The internal length is $l_0 = 0.0075$ mm, toughness $G_c = 2.7 \cdot 10^{-3}$ kN/mm, Young modulus $E = 210$ kN/mm$^2$, and Poisson ratio $\nu = 0.3$. The displacement-control loading history is characterized by a maximum displacement $u_{max} = 6 \cdot 10^{-3}$ mm and features a non-uniform load increment: $\Delta u = 10^{-4}$ mm from $u = 0$ mm to $u = 4 \cdot 10^{-3}$ mm and then $\Delta u = 10^{-5}$ mm until the end. The analyses are performed with quadratic $C^1$-continuous shape functions and locally refined (tensor-product) meshes. Namely, for the second-order functional with $h = l_0/4$, the minimum element size is 0.00125 mm in the area where the fracture propagates (see Fig. 11) and maximum element size of 0.0125
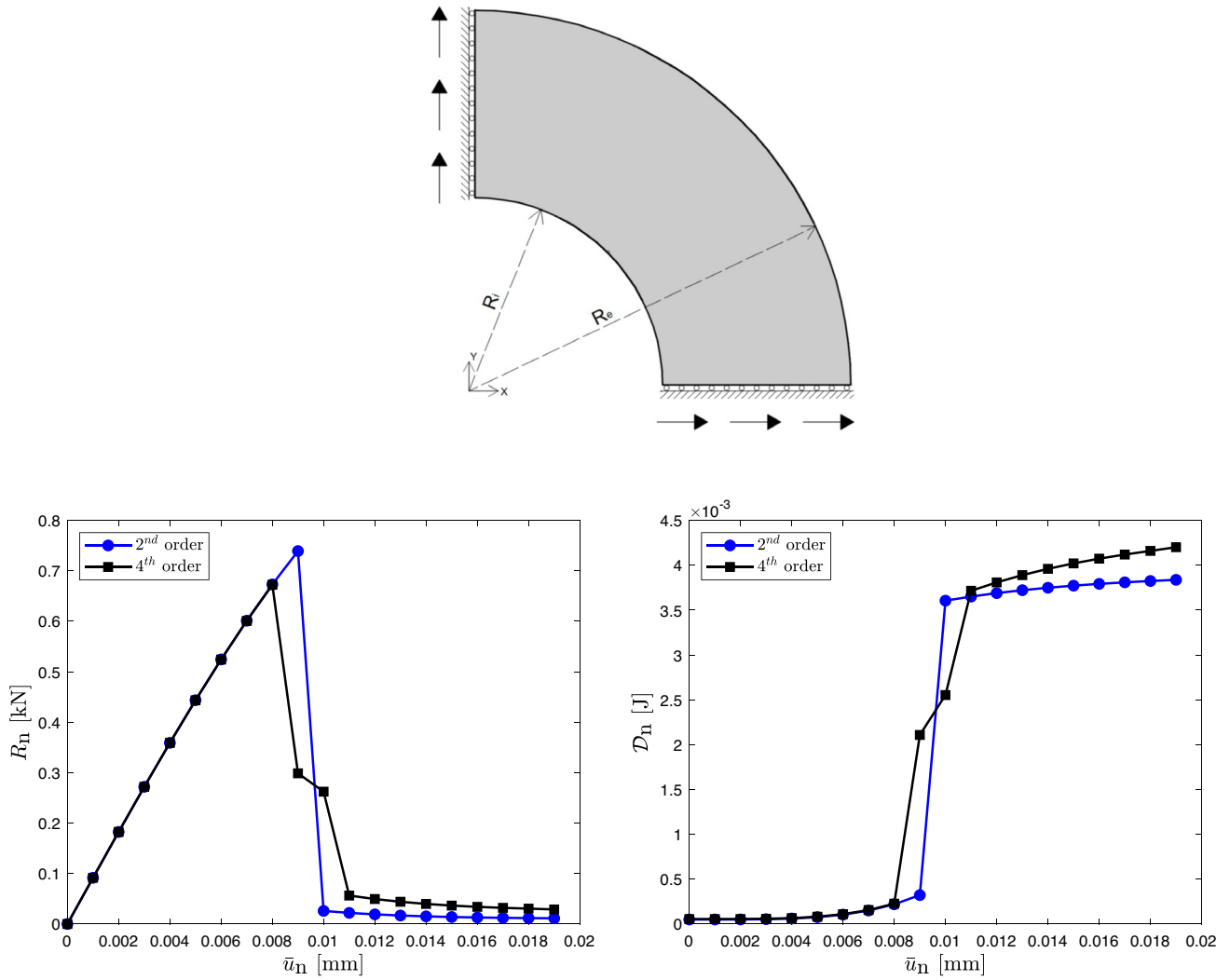
**Fig. 8** Quarter of Annulus test. Top row: geometry and boundary conditions. Bottom row: from left to right, reaction and dissipated energy curves obtained comparing the second-order formulation using $h = l_0/8$ and the fourth-order one with $h = l_0/4$

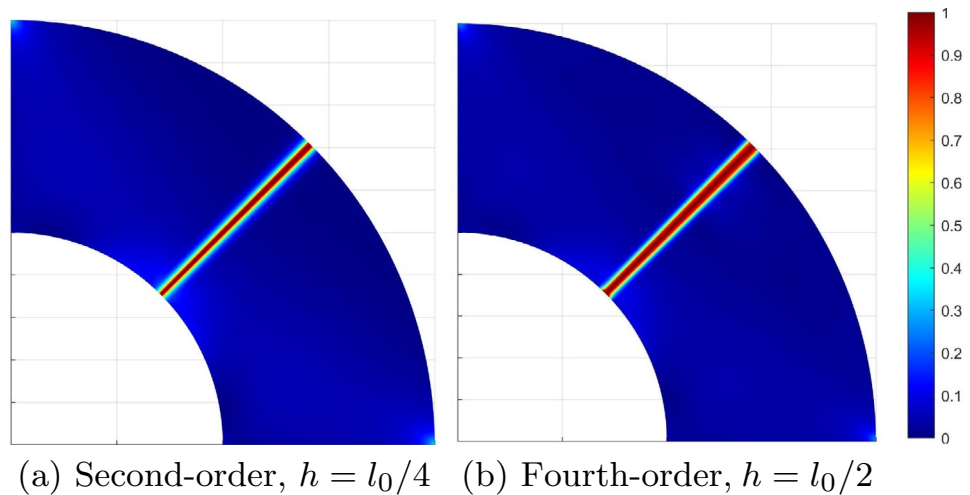**Fig. 9** Quarter of annulus test, total breakage crack pattern



(a) Second-order, $h = l_0/4$    (b) Fourth-order, $h = l_0/2$

**Table 8** Mesh features

| $h$ | Elements | Control points |
| --- | --- | --- |
| [mm] | [–] | [–] |
| $l_0/2$ | 10,000 | 10,404 |
| $l_0/4$ | 40,000 | 40,804 |
| $l_0/6$ | 90,000 | 91,204 |
| $l_0/8$ | 160,000 | 161,604 |

**Table 9** Quarter of annulus: second-order model accuracy evaluation

| $h$ | $G_c^{Eff}$ | $\Delta G_c^{Eff}$ | Conv. rate | Error | Time |
| --- | --- | --- | --- | --- | --- |
| [mm] | [kN/mm] | [kN/mm] | [-] | [%] | [h: min] |
| $l_0/2$ | $5.427 \cdot 10^{-3}$ | $2.727 \cdot 10^{-3}$ | – | 100.0 | 01:39 |
| $l_0/4$ | $3.988 \cdot 10^{-3}$ | $1.288 \cdot 10^{-3}$ | 1.082 | 47.7 | 04:43 |
| $l_0/6$ | $3.544 \cdot 10^{-3}$ | $8.440 \cdot 10^{-3}$ | 1.042 | 31.3 | 13:14 |
| $l_0/8$ | $3.283 \cdot 10^{-3}$ | $5.830 \cdot 10^{-3}$ | 1.286 | 21.6 | 36:19 |

**Table 10** Quarter of annulus: fourth-order model accuracy evaluation

| $h$ | $G_c^{Eff}$ | $\Delta G_c^{Eff}$ | Conv. rate | Error | Time |
| --- | --- | --- | --- | --- | --- |
| [mm] | [kN/mm] | [kN/mm] | [-] | [%] | [h: min] |
| $l_0/2$ | $4.735 \cdot 10^{-3}$ | $2.035 \cdot 10^{-3}$ | – | 75.4 | 01:28 |
| $l_0/4$ | $3.488 \cdot 10^{-3}$ | $7.881 \cdot 10^{-3}$ | 1.368 | 29.2 | 06:32 |
| $l_0/6$ | $3.147 \cdot 10^{-3}$ | $4.470 \cdot 10^{-3}$ | 1.399 | 16.6 | 09:28 |
| $l_0/8$ | $2.936 \cdot 10^{-3}$ | $2.360 \cdot 10^{-3}$ | 2.220 | 9.00 | 29:31 |
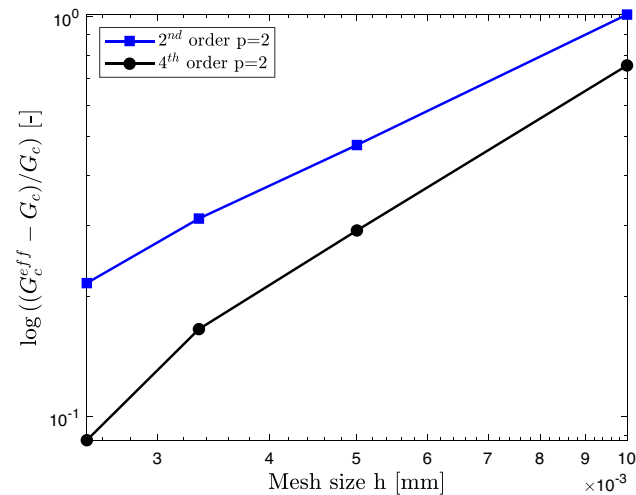


**Fig. 10** Quarter of Annulus test. Relative error *versus* mesh size $h \in \{l_0/2, l_0/4, l_0/6, l_0/8\}$

mm away from the propagation area. Instead, for the fourth-order functional with $h = l_0/2$ the minimum element size is 0.0025 mm in the area where the fracture propagates while

maximum element size is equal to 0.025 mm away from the propagation area.

This test presents two non-aligned pre-cracks. They are positioned at $\pm 0.03$ mm with respect to the x-axis and they are 0.2 mm long. To reduce the computational effort, the geometry is scaled down with respect to the one proposed by Molnar et al. [22]. Geometry and boundary conditions are then summarized in Fig. 11.

In Fig. 12, we compare the crack patterns corresponding to the final step for the second- and fourth-order functionals. It can be seen that the fourth-order model captures the coalescence phenomenon well even when considering a mesh size $h$ that is twice the one of the second-order model, resulting in a wider crack. We highlight that this leads to a computational effort that is significantly reduced; in fact the fourth-order analysis with the coarsest mesh requires only 4 h 37 min while the second-order simulation with the finest mesh and comparable expected level of accuracy needs 22 h 01 min, entailing an 80% reduction in term of total time required by the analysis for the fourth-order model.

## 5 Conclusions

In this work, we provide an exhaustive comparison of a second- and a fourth-order formulations for phase-field brittle fracture. The investigated fourth-order model presents a higher order differential operator that can be discretized in a straightforward manner relying on the highly continuous properties of IgA shape functions, highlighting once again the flexibility of IgA in the context of modeling high order PDEs. We consider several benchmarks, with different level of complexity in terms of geometry and fracture patterns and compare the accuracy of the two considered formulations for different mesh sizes. For the same mesh, the fourth-order model is always more accurate than the second-order one, while we observe a comparable accuracy with meshes typically twice coarser for the fourth-order model. This turns into a remarkable reduction in terms of total computational time required by the overall analysis. Inspired by the native field of application of Mumford–Shah functional, to compute the effective toughness in the error measure assessment, we propose to evaluate the crack length by means of an image-based algorithm that allows to measure the fracture length also for complex patterns. Furthermore, we investigate a different strategy to impose the initial pre-field that gives higher accuracy results with respect to a state-of-the-art method. As the examined fourth-order formulation, once spatially discretized, turns out to be a SLCP, we propose to handle the irreversibility condition in a straightforward and rigorous manner using the PSOR scheme [8]. Among future works, we plan to consider the combination of the fourth-order phase-field formulation with other types of structures such as Kirchhoff–Love shells, also requiring $C^1$-continuity, as well as

**Fig. 11** Asymmetric double pre-notch [22]. Left: geometry and boundary conditions. Right: local refinement strategy
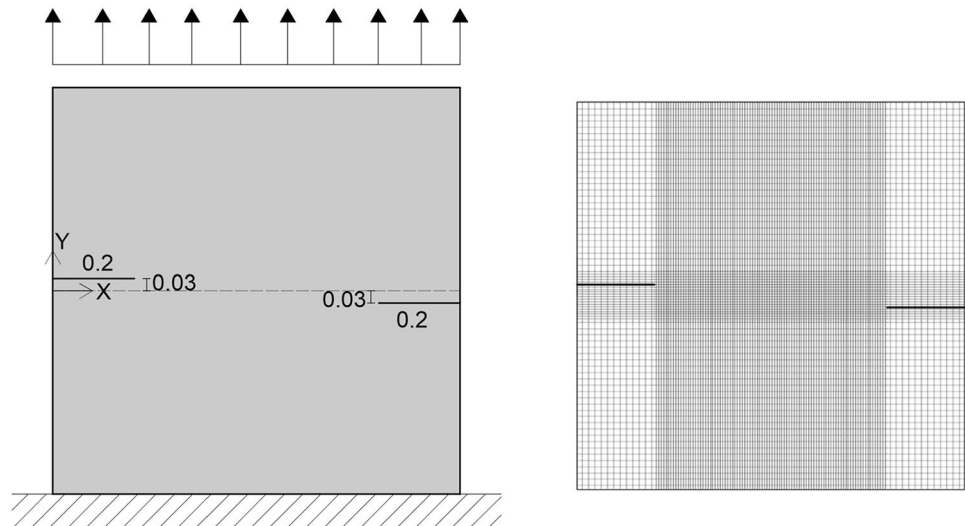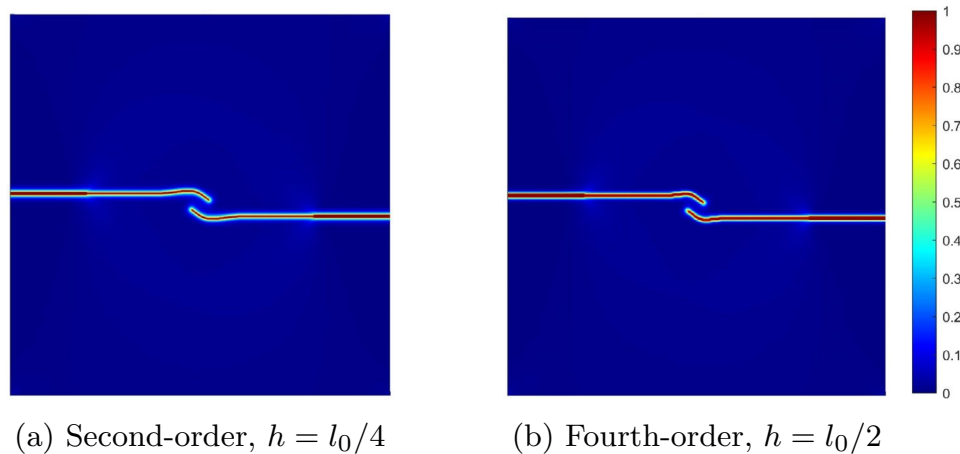


**Fig. 12** Asymmetric double pre-notch. Crack pattern corresponding to the final loading step



(a) Second-order, $h = l_0/4$      (b) Fourth-order, $h = l_0/2$

to investigate the influence of the higher-order term in dynamic problems. Furthermore, we will analyze higher-order formulations in the context of the AT1 model, where the aim will be to combine the computational advantage given by high-order formulations with the properties of the AT1 model, that, in contrast to AT2, introduces an elastic limit in the material.

Finally, among further developments we highlight the extension of this simulation framework to THB-splines adaptivity and multi-patch geometries [24].

# Appendix A: Techniques to impose an initial phase-field pre-field condition

## Pre-field imposition *via* History variable

We briefly recall the $\mathcal{H}_0$ method proposed in [9] that is our starting point to impose an optimal initial phase-field solution at the control points $\hat{\mathbf{d}}_0$. Therefore, the initial strain history field $\mathcal{H}_0$ readapted for the adopted phase-field variable convention (i.e., d = 0 undamaged material and d = 1 fully broken material) is

$$\mathcal{H}_0 = B \begin{cases} \frac{G_c}{2\,l_0}(1 - \frac{\rho(\mathbf{x},l)}{\beta}) & \rho(\mathbf{x},l) \leq \beta \\ 0 & \rho(\mathbf{x},l) > \beta, \end{cases} \tag{27}$$

where $\rho(\mathbf{x}, l)$ is the distance function from $\mathbf{x}$ to the discrete crack $l$ we intend to model. Thus, the value of $B$ in Eq. (27) can be derived substituting $\mathcal{H}_0$ into Euler equation for $\rho = 0$ (see Appendix A in Borden et al. [9] for further details) obtaining:

$$-l_0\nabla^2 d + d = \frac{2l_0}{G_c}(1 - d)\mathcal{H}_0, \tag{28}$$

and, thereby neglecting the high-order term $\nabla^2 d$, we obtain the following simplified expression:

**Fig. 13** From left to right: geometry and boundary conditions for the Centre-Cracked Plate Test, IPF *versus* $\mathcal{H}_0$ methods for second-order phase-field modeled with $C^1$-continuous shape functions
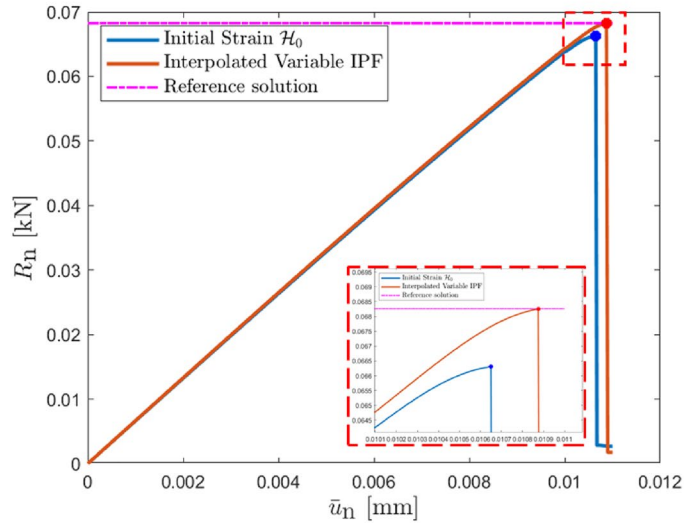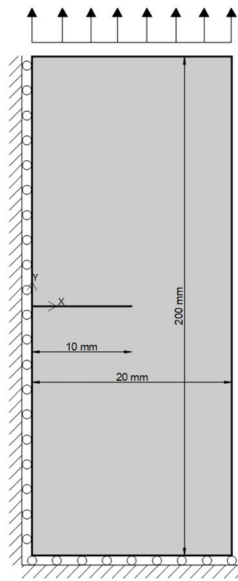


$$d = \frac{2l_0}{G_c}(1 - d)\mathcal{H}_0 = (1 - d)B. \tag{29}$$

Then, it follows that

$$B = \frac{c}{1 - c}, \tag{30}$$

where we have defined $c$ depending on the considered problem mesh size $h$. Namely, for a bivariate problem, if $h = \frac{l_0}{\mathrm{nel}_{l_0}} \approx 10^{-k}$ (i.e., $\mathrm{nel}_{l_0}$ is the number of elements that resolves $l_0$ and $k \in \mathbb{N}$), we take $c = 1 - 10^{-(k+1)}$. For example, if $\mathrm{nel}_{l_0} = 4$ and $l_0 = 0.01$ mm, we have that $h = \frac{0.01}{4} = 2.5 \cdot 10^{-3}$ mm and therefore $k = 3$ and $c = 1 - 10^{-(4)} = 0.9999$. Now that $\mathcal{H}_0$ is defined, we highlight in Eq. (27) that the distance $\rho$ is limited by the parameter $\beta$ which is set to be equal to the mesh size $h$ (namely, in the considered SEN cases in Section (4) we "activate" one row of elements). Thus, to obtain the optimal initial phase-field solution at the control points $\hat{\mathbf{d}}_0$, we substitute $\psi^+$ with $\mathcal{H}_0$ definition (27) into Eq. (7) for the second-order and Eq. (9) for the fourth-order which turn out to be in both cases linear systems in $\hat{\mathbf{d}}_0$ once spatially discretized. The computed value of $\hat{\mathbf{d}}_0$ becomes then the staggered phase-field initial condition at step 0 (see point 2 in Algorithm 2 in Appendix C).

## Pre-field imposition on the interpolated phase-field variable

All the analyses considered in this work are carried out within an IgA framework. Therefore an initial phase-field solution corresponding to a pre-crack should be imposed on the interpolated phase-field variable rather than at the control points. Thus, we impose the pre-field inside the domain through an $L^2$-projection. The projection is carried out by means of a matrix $(\mathbf{M})_{\mathbf{ij}} = \int_{\Omega} R_{\mathbf{i,p}} R_{\mathbf{j,p}} \, d\Omega$ and a vector $\left(\mathbf{F}_{\mathrm{d}}\right)_{\mathbf{i}} = \int_{\Omega} R_{\mathbf{i,p}} c \, d\Omega$, where $c$ is the value of the phase-field variable at the Gauss-point that we imposed equal to 0.9999 (i.e., actual value corresponding to fully broken material state) near the discontinuity and 0 elsewhere. It follows that the pre-field $\hat{\mathbf{d}}_0$ is computed as the solution of the linear system:

$$\mathbf{M} \cdot \hat{\mathbf{d}}_0 = \mathbf{F}_{\mathrm{d}}. \tag{31}$$

Then, we test the introduced IPF technique against the $\mathcal{H}_0$ method considering the Centre-Cracked Plate test [23]. For this benchmark, we consider the second-order phase-field model introduced in Eq. (7). The sample has a rectangular geometry of 20x200 mm with an initial crack length $a_0 = 10$ mm located at $y = 0$ and presents internal length $l_0 = 0.5$ mm [16], toughness $G_c = 7 \cdot 10^{-6}$ kN/mm, Young modulus $E = 7 \cdot 10^4$ kN/mm$^2$, and Poisson ratio $\nu = 0.22$. The displacement-control load history is characterized by a maximum displacement $u_{max} = 12 \cdot 10^{-3}$ mm and an adaptive load increment as follows: $\Delta u = 2.5 \cdot 10^{-4}$ mm from $u_{min}$ until $u = 10^{-1}$ mm and $\Delta u = 2.5 \cdot 10^{-5}$ mm from $u = 10^{-1}$ mm until the final loading step. All analyses for this benchmark are performed with quadratic $C^1$-continuous shape functions, a uniform mesh of 64,000 elements and 65,764 control points.

As we can observe from Fig. 13 and Table 11, the IPF exhibits a relative error that in this case is 1/50 of the one obtained with the $\mathcal{H}_0$ method, thereby providing a good alternative to the $\mathcal{H}_0$ technique.

**Table 11** Pre-field imposition comparison in Centre-Cracked Plate test

| Method | Peak reaction [kN] | Error [%] |
|---|---|---|
| $\mathcal{H}_0$ [9] | $6.63 \cdot 10^{-2}$ | 2.87 |
| IPF | $6.83 \cdot 10^{-2}$ | 0.06 |
| Analytical [23] | $6.83 \cdot 10^{-2}$ | – |

## Appendix B: Image-based algorithm to measure the crack length of complex patterns

As pointed out in Eq. (24), the evaluation of the crack length has a crucial role to study the accuracy of the investigated formulations. Therefore, inspired by the native field of application of Mumford–Shah functional [25], i.e., image segmentation, we propose an algorithm to assess the fracture length by means of an imaging technique.

The algorithm detailed in Algorithm 1 is implemented in MATLAB. In this case the input file has extension "*.fig" and presents the same pixel numbers in x and y direction. From the input file (1), a matrix containing the figure information is obtained. From this variable, the image background, related to the blue that represents the entire material, is set as black and then a greyscale figure is obtained (2) by averaging the three color channels R, G, and B. Thanks to this procedure, a unique intensity value related to the grey level of each pixel is obtained. This value is between 0 and 1: 0 corresponds, with the conventions introduced in the previous sections, to the unbroken material, while 1 represents the fully damaged material state. This greyscale figure is the starting point for the binarization process of the figure (3). This is done by considering a threshold, that allows us to set equal to 1 all the pixels that have a value higher than the established threshold. In this way, we can identify an object composed by pixels that only have a value equal to 1 representing the fracture: the higher the threshold value, the smaller the thickness of the obtained binary object. Performing several tests, it was observed that to get a faithful representation of the fracture, this threshold should be chosen between values 0.7 and 0.85. From the binarized object we can obtain the skeleton of the fracture (4) relying on the the so-called skeletonization algorithm that extrapolates the skeleton of a 2D figure identified by curve. The last two steps consist of measuring the line and converting it to millimeters (for the units of measure chosen in our tests). The length of the line is calculated as half the perimeter of the skeleton. We emphasize the importance of considering half the length, because the MATLAB function "regionprops" [26] calculates the perimeter of the object, which is twice the length of the line. Finally, the obtained measurement is converted from pixels to, e.g., millimeters.

**Algorithm 1** Image-based algorithm to measure the crack length of complex patterns

**Input:** High resolution crack pattern contour plot
1: Convert input image into an RGB matrix ($im_{RGB}$)
2: Convert the RGB figure into a gray scale image $im_{GS}$
3: $im_{GS} = \text{mean}(im_{RGB}, 3)$
4: Binarize the image using a threshold for the gray scale ($TH_G$)
5: $im_{GS} > TH_G \rightarrow im_{BIN} = im_{GS}$
6: Compute the so called "skeleton object"
7: $sk = \text{bwskel}(im_{BIN})$
8: Compute the perimeter of the object
9: $rp = \text{regionprops}(sk, \text{'Perimeter'})$
10: Compute the length of the fracture in [px]
11: $a = 0.5 \cdot rp.\text{Perimeter}$
12: Convert crack length $a$ from [px] into [L] (e.g., [mm])
**Output:** Length of fracture $a$ in [mm]

The pixel length side is calculated by means of a proportion depending on the resolution of the utilized monitor. For example in the considered SEN shear test [7], displayed in Fig. 14, 1 mm is equivalent to 762 pixels considering a 15.6" monitor with a resolution of $1920 \times 1080$ pixels. Furthermore we highlight in Fig. 14 that this technique can easily capture complicated fracture patterns, namely cracks that feature changes in slope and curves with an error of four pixels in the origin of the axes, correspond to $1.31 \cdot 10^{-3}$ mm.

## Appendix C: Staggered algorithm features

The adopted staggered algorithm is sketched more specifically in Algorithm 2 for a fixed loading step n ≥ 1: first, we tackle the non-linearity given by the energy split employing a classical Newton–Raphson scheme that checks the $L^2$-norm of the discretized balance of linear momentum $\partial_\mathbf{u}\Pi$. Therefore, for every $j$th Newton–Raphson iteration we control

$$\text{Res}_{NR,\mathbf{u}}^j = \|\partial_\mathbf{u}\Pi(\mathbf{u}^j, d^{i-1})\|_{L^2} < TOL_{NR,\mathbf{u}}, \qquad (32)$$

where $TOL_{NR,\mathbf{u}} = 10^{-9}$ kJ, according to [27], until convergence and then, if criterion (32) is met, we set $\mathbf{u}^i = \mathbf{u}^j$. Conversely, to handle the nonlinearity stemming from the constrained minimization problem, we utilize the PSOR algorithm [5, 21], as addressed in Sect. 3.3, after the spatial discretization of the system of equations. To control the convergence of the algorithm, we check the $L^\infty$-norm of the variation of the phase-field increment at the control points between two subsequent iterations $k-1$ and $k$:

$$\text{Res}_{PSOR,\Delta d}^k = \|\Delta d^k - \Delta d^{k-1}\|_{L^\infty} < TOL_{PSOR,\Delta d},$$

**Fig. 14** Fracture skeleton (yellow line) superimposed to the original binarized image (see top-left figure). From the top-right figure following the reported numbering order: details of the initial zone, point of curvature, and final part of the fracture, respectively
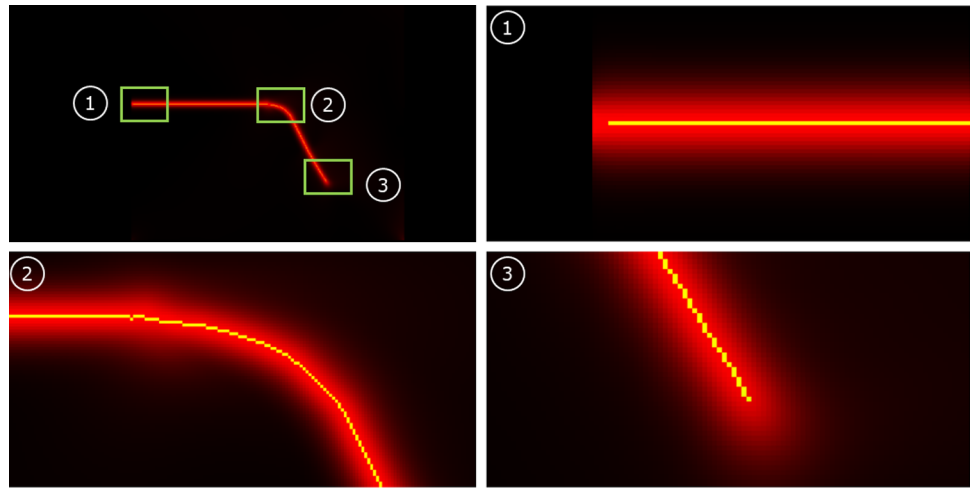


where $\mathtt{TOL}_{\mathrm{PSOR},\Delta d} = 10^{-4}$ [8], thereby setting $\Delta d^i = \Delta d^k$ and updating the new staggered $i$-th phase-field solution $d^i = d_{n-1} + \Delta d^i$. Since the adopted staggered algorithm is structured so that we first solve the balance of linear momentum, after the solution of the phase-field problem our exit criterion controls that the $L^2$- norm of the out-of-balance work is lower than a prescribed tolerance, namely:

$$\mathrm{Res}_{\mathrm{stag}} = \|\partial_{\mathbf{u}}\Pi(\mathbf{u}^i, d^i)[\Delta\mathbf{u}^i]\|_{L^2} < \mathtt{TOL}_{\mathrm{stag}},$$

where $\mathtt{TOL}_{\mathrm{stag}} = 10^{-7}\,\mathrm{kJ}$ (see [27]).

**Algorithm 2** Staggered iteration algorithm for $n \geq 1$

---

**Input:** load solution $(\mathbf{u}_{n-1}, d_{n-1})$ from step $n-1$ and boundary conditions $\bar{\mathbf{u}}_n$, $\mathbf{t}_n$ at current step $n$
1: initialize $i = 0$
2: set $(\mathbf{u}^0, d^0) := (\mathbf{u}_{n-1}, d_{n-1})$
3: **while** $\mathrm{Res}_{\mathrm{stag}} \geq \mathtt{TOL}_{\mathrm{stag}}$ **do**
4:     $i \to i+1$
5:     given $d^{i-1} = d_{n-1} + \Delta d^{i-1}$, find $\mathbf{u}^i$ solving $\partial_{\mathbf{u}}\Pi(\mathbf{u}^i, d^{i-1}) = \mathbf{0}$
6:     given $\mathbf{u}^i$, find $\Delta d^i$ solving $\partial_d \Pi^{ii,iv}(\mathbf{u}^i, d^i)[\Delta d^i] = 0$ with $\partial_d \Pi^{ii,iv}(\mathbf{u}^i, d^i) \geq 0$, $\Delta d^i \geq 0$
7:     compute $\mathrm{Res}_{\mathrm{stag}} = \|\partial_{\mathbf{u}}\Pi(\mathbf{u}^i, d^i)[\Delta\mathbf{u}^i]\|_{L^2}$
8: **end while**
9: $(\mathbf{u}_n, d_n) \to (\mathbf{u}^i, d^i)$
**Output:** $(\mathbf{u}_n, d_n)$

---

**Data availability** The data that support the findings of this study are available from the authors upon reasonable request.

## Declarations

**Conflict of interest** The authors have no conflicts of interest to declare that are relevant to the content of this article.

# References

1. Griffith AA, Taylor GI (1921) Vi the phenomena of rupture and flow in solids. Philos Trans R Soc Lond Ser A Contain Pap Math Phys Char 221(582–593):163–198. https://doi.org/10.1098/rsta.1921.0006

2. Francfort GA, Marigo J-J (1998) Revisiting brittle fracture as an energy minimization problem. J Mech Phys Solids 46(8):1319–1342. https://doi.org/10.1016/S0022-5096(98)00034-9

3. Bourdin B, Francfort GA, Marigo J-J (2000) Numerical experiments in revisited brittle fracture. J Mech Phys Solids 48(4):797–826. https://doi.org/10.1016/S0022-5096(99)00028-9

4. Ambrosio L, Tortorelli VM (1990) Approximation of functional depending on jumps by elliptic functional via t-convergence. Commun Pure Appl Math 43(8):999–1036. https://doi.org/10.1002/cpa.3160430805

5. Comi C, Perego U (2001) Fracture energy based bi-dissipative damage model for concrete. Int J Solids Struct 38(36):6427–6454. https://doi.org/10.1016/S0020-7683(01)00066-X

6. Miehe C, Welschinger F, Hofacker M (2010) Thermodynamically consistent phase-field models of fracture: Variational principles and multi-field fe implementations. Int J Numer Meth Eng 83(10):1273–1311. https://doi.org/10.1002/nme.2861

7. Gerasimov T, De Lorenzis L (2019) On penalization in variational phase-field models of brittle fracture. Comput Methods Appl Mech Eng 354:990–1026. https://doi.org/10.1016/j.cma.2019.05.038

8. Marengo A, Patton A, Negri M, Perego U, Reali A (2021) A rigorous and efficient explicit algorithm for irreversibility enforcement in phase-field finite element modeling of brittle crack propagation. Comput Methods Appl Mech Eng 387:114137. https://doi.org/10.1016/j.cma.2021.114137

9. Borden MJ, Verhoosel CV, Scott MA, Hughes TJR, Landis CM (2012) A phase-field description of dynamic brittle fracture. Comput Methods Appl Mech Eng 217–220:77–95. https://doi.org/10.1016/j.cma.2012.01.008

10. Borden MJ, Hughes TJR, Landis CM, Verhoosel CV (2014) A higher-order phase-field model for brittle fracture: Formulation and analysis within the isogeometric analysis framework. Comput Methods Appl Mech Eng 273:100–118. https://doi.org/10.1016/j.cma.2014.01.016

11. Negri M (2020) $\gamma$-convergence for high order phase field fracture: Continuum and isogeometric formulations. Comput Methods Appl Mech Eng 362:112858. https://doi.org/10.1016/j.cma.2020.112858

12. Hughes TJR, Cottrell JA, Bazilevs Y (2005) Isogeometric analysis: Cad, finite elements, nurbs, exact geometry and mesh refinement. Comput Methods Appl Mech Eng 194(39):4135–4195. https://doi.org/10.1016/j.cma.2004.10.008

13. Nguyen-Thanh N, Li W, Huang J, Zhou K (2020) Adaptive higher-order phase-field modeling of anisotropic brittle fracture in 3d polycrystalline materials. Comput Methods Appl Mech Eng 372:113434. https://doi.org/10.1016/j.cma.2020.113434

14. Schillinger D, Borden MJ, Stolarski HK (2015) Isogeometric collocation for phase-field fracture models. Comput Methods Appl Mech Eng 284:583–610. https://doi.org/10.1016/j.cma.2014.09.032

15. Nguyen KD, Augarde CE, Coombs WM, Nguyen-Xuan H, Abdel-Wahab M (2020) Non-conforming multipatches for NURBS-based finite element analysis of higher-order phase-field models for brittle fracture. Eng Fract Mech 235:107133. https://doi.org/10.1016/j.engfracmech.2020.107133

16. Goswami S, Anitescu C, Rabczuk T (2020) Adaptive fourth-order phase field analysis for brittle fracture. Comput Methods Appl Mech Eng 361:112808. https://doi.org/10.1016/j.cma.2019.112808

17. Proserpio D, Ambati M, De Lorenzis L, Kiendl J (2020) A framework for efficient isogeometric computations of phase-field brittle fracture in multipatch shell structures. Comput Methods Appl Mech Eng 372:113363. https://doi.org/10.1016/j.cma.2020.113363

18. Amor H, Marigo J-J, Maurini C (2009) Regularized formulation of the variational brittle fracture with unilateral contact: Numerical experiments. J Mech Phys Solids 57(8):1209–1229. https://doi.org/10.1016/j.jmps.2009.04.011

19. Piegl L, Tiller W (1996) The NURBS Book, 2nd edn. Springer, New York, NY, USA

20. Cottrell JA, Hughes TJR, Reali A (2007) Studies of refinement and continuity in isogeometric structural analysis. Comput Methods Appl Mech Eng 196(41):4160–4183. https://doi.org/10.1016/j.cma.2007.04.007

21. Mangasarian OL (1977) Solution of Symmetric Linear Complementarity Problems by Iterative methods. J Optim Theory Appl 22:465–485. https://doi.org/10.1007/BF01268170

22. Molnár G, Gravouil A (2017) 2d and 3d abaqus implementation of a robust staggered phase-field solution for modeling brittle fracture. Finite Elem Anal Des 130:27–38. https://doi.org/10.1016/j.finel.2017.03.002

23. Sargado JM, Keilegavlen E, Berre I, Nordbotten JM (2018) High-accuracy phase-field models for brittle fracture based on a new family of degradation functions. J Mech Phys Solids 111:458–489. https://doi.org/10.1016/j.jmps.2017.10.015

24. Bracco C, Giannelli C, Reali A, Torre M, Vázquez R (2023) Adaptive isogeometric phase-field modeling of the cahn-hilliard equation: Suitably graded hierarchical refinement and coarsening on multi-patch geometries. Comput Methods Appl Mech Eng 417:116355. https://doi.org/10.1016/j.cma.2023.116355

25. Mumford DB, Shah J (1989) Optimal approximations by piecewise smooth functions and associated variational problems. Commun Pure Appl Math. https://doi.org/10.1002/cpa.3160420503

26. MATLAB: 9.7.0.1190202 (R2019b) (2018) The MathWorks Inc., Natick, Massachusetts

27. Gerasimov T, De Lorenzis L (2016) A line search assisted monolithic approach for phase-field computing of brittle fracture. Comput Methods Appl Mech Eng 312:276–303. https://doi.org/10.1016/j.cma.2015.12.017